The effects of explicit versus parameterized convection on the MJO in a large-domain high-resolution tropical case study. Part II: Processes leading to differences in MJO development

Holloway, C. E. ORCID: https://orcid.org/0000-0001-9903-8989, Woolnough, S. J. ORCID: https://orcid.org/0000-0003-0500-8514 and Lister, G. M. S. (2015) The effects of explicit versus parameterized convection on the MJO in a large-domain high-resolution tropical case study. Part II: Processes leading to differences in MJO development. Journal of the Atmospheric Sciences, 72 (7). pp. 2719-2743. ISSN 1520-0469 doi: 10.1175/JAS-D-14-0308.1 Available at https://centaur.reading.ac.uk/39881/

To link to this article DOI: http://dx.doi.org/10.1175/JAS-D-14-0308.1

Publisher: American Meteorological Society

The Effects of Explicit versus Parameterized Convection on the MJO in a Large-Domain High-Resolution Tropical Case Study. Part II: Processes Leading to Differences in MJO Development*

CHRISTOPHER E. HOLLOWAY AND STEVEN J. WOOLNOUGH

Climate, National Centre for Atmospheric Science, Department of Meteorology, University of Reading, Reading, United Kingdom

GRENVILLE M. S. LISTER

Computational Modelling Support, National Centre for Atmospheric Science, Department of Meteorology, University of Reading, Reading, United Kingdom

(Manuscript received 17 October 2014, in final form 20 February 2015)

ABSTRACT

High-resolution simulations over a large tropical domain (~20°S–20°N, 42°E–180°) using both explicit and parameterized convection are analyzed and compared during a 10-day case study of an active Madden–Julian oscillation (MJO) event. In this paper, Part II of this study, the moisture budgets and moist entropy budgets are analyzed. Vertical subgrid diabatic heating profiles and vertical velocity profiles are also compared; these are related to the horizontal and vertical advective components of the moist entropy budget, which contribute to gross moist stability (GMS) and normalized GMS (NGMS). The 4-km model with explicit convection and good MJO performance has a vertical heating structure that increases with height in the lower troposphere in regions of strong convection (like observations), whereas the 12-km model with parameterized convection and a poor MJO does not show this relationship. The 4-km explicit convection model also has a more top-heavy heating profile for the troposphere as a whole near and to the west of the active MJO-related convection, unlike the 12-km parameterized convection model. The dependence of entropy advection components on moisture convergence is fairly weak in all models, and differences between models are not always related to MJO performance, making comparisons to previous work somewhat inconclusive. However, models with relatively good MJO strength and propagation have a slightly larger increase of the vertical advective component with increasing moisture convergence, and their NGMS vertical terms have more variability in time and longitude, with total NGMS that is comparatively larger to the west and smaller to the east.

1. Introduction

In the first part of this paper (Holloway et al. 2013, hereafter H13), we presented results comparing six large-domain limited-area Met Office Unified Model (MetUM) simulations of a 10-day Madden–Julian oscillation (MJO) case beginning on 6 April 2009. We found that explicit convection simulations with both 4- and 12-km grid spacing produce a stronger, more realistic MJO signal with more eastward propagation than 12- and 40-km parameterized convection simulations, which have much less MJO amplitude and propagation. In H13, as well as in a previous paper analyzing four of these simulations (Holloway et al. 2012, hereafter H12), the improved MJO in three of the explicit convection simulations was linked to a more realistic relationship between precipitation and lower-free-tropospheric moisture, as well as increased generation of available potential energy and conversion of that energy into kinetic energy. The increased energetics terms were, in turn, linked to larger zonal variance in convective heating and vertical velocity (which corresponds to higher probabilities of high precipitation rates at 1° latitude–longitude, 3-hourly scales found in all

---

Denotes Open Access content.

---

* Supplemental information related to this paper is available at the Journals Online website: http://dx.doi.org/10.1175/JAS-D-14-0308.s1.

Corresponding author address: Christopher E. Holloway, Department of Meteorology, University of Reading, Earley Gate, P.O. Box 243, Reading RG6 6BB, United Kingdom.
E-mail: c.e.holloway@reading.ac.uk

DOI: 10.1175/JAS-D-14-0308.1

explicit convection simulations in H12), larger zonal 200-hPa temperature variance, and larger midtropospheric correlations between temperature and ascent (and between temperature and diabatic heating).

In this paper, we investigate the vertical heating structures, moisture budgets, and moist entropy budgets of several of these simulations, particularly the 4-km simulation with Smagorinsky subgrid mixing in all three dimensions (4-km 3Dsmag), which had the overall best MJO, and the 12-km simulation with parameterized convection (12-km param), which had a poor MJO. We also show some analysis for two more simulations of this case using the convective parameterization with 1.5 times the mixing entrainment (and mixing detrainment) rate of the other parameterized convection runs (12-km 1.5ent and 40-km 1.5ent) based on findings in Klingaman and Woolnough (2014) that global simulations with this change had an improved MJO. Our motivation to investigate the vertical diabatic heating structures along with the moisture and moist entropy budgets comes from a growing consensus in the community that the MJO behaves like a "moisture mode" (e.g., Grabowski and Moncrieff 2004; Raymond and Fuchs 2009; Sobel and Maloney 2013; Pritchard and Bretherton 2014). A moisture-mode mechanism for the MJO relies on increased moist entropy (or moist static energy) in the active convective region and tendencies that increase moist entropy to the east of this region and decrease moist entropy to the west.

The moisture budget can give insight into moisture-mode mechanisms, since moisture variability accounts for most moist entropy variability in the deep tropics (e.g., DeMott et al. 2014). However, the moist entropy budget has the advantage that phase changes of water, and relatedly, precipitation, do not appear as terms. Instead, source–sink terms from surface heat fluxes and radiation are mostly balanced by advection. The vertically integrated net advection of moist entropy from a region, normalized by the vertically integrated moisture convergence (MC) in that region, is called the normalized gross moist stability (NGMS) and has been found to be related to MJO performance in some models (Hannah and Maloney 2014; Benedict et al. 2014; Jiang et al. 2015). This is related to the original gross moist stability first defined by Neelin and Held (1987), although it uses moist entropy rather than moist static energy, normalizes by MC, and includes both vertical and horizontal advective terms. The vertical advective term will depend on the vertical profile of moist entropy and the vertical profile of vertical velocity, which, in turn, is related to diabatic heating and vertical stability in the tropics. This links our interest in vertical heating structures and related fields, such as vertical velocity and stability, to the moisture-mode theory.

The moisture-mode theory has gained traction in recent years, partly because there have been a number of studies of general circulation models (GCMs) that show markedly improved MJO amplitude and propagation when the convective parameterizations are altered to increase the sensitivity of convection to free-tropospheric moisture, usually by increasing entrainment or increasing subsaturated downdrafts (e.g., Tokioka et al. 1988; Hannah and Maloney 2011; Kim et al. 2012; Hirons et al. 2013; Klingaman and Woolnough 2014; Benedict et al. 2014). However, in many of these simulations with improved MJO activity, there is an unfortunate reduction in the fidelity of the climatological mean state in the tropics (Mapes and Neale 2011; Kim et al. 2011). Also, Benedict et al. (2014) have argued that two GCMs with traditional convective parameterizations that have been altered to increase convective sensitivity to moisture might be getting an improved MJO for the wrong reasons, when compared with both the ECMWF interim reanalysis (ERA-Interim) and the Superparameterized Community Atmosphere Model (SPCAM), which uses 2D explicit convection models embedded inside each GCM grid box and has an improved MJO over the normal Community Atmosphere Model (CAM). Benedict et al. (2014) find that the two convectional GCMs with altered convection schemes have different relationships between the vertical and horizontal components of moist entropy advection to MC than SPCAM and ERA-Interim (as well as a somewhat different relationship between radiative fluxes and MC), although the relationship between total advective increments of moist entropy and MC are similar among all four. One interpretation of these findings is that, at least for those two models with altered convection schemes, it might be a cancellation of errors that was leading to an improved MJO. Hannah and Maloney (2014) also study GCMs with increased entrainment in a moisture mode framework, and they come to a similar conclusion that these modified GCMs get a good MJO for the wrong reasons, having a too-strong import of moist entropy via vertical advection that cancels out a too-weak radiative–convective feedback and a too-strong export of moist entropy via horizontal advection. Improving the relevant processes in models to reduce these errors might then allow for a better MJO, along with improved convection in general and even an improved mean state.

Our simulations, part of the U.K. Cascade project, allow for comparison between simulations with parameterized and explicit convection for similar lateral boundary conditions. By representing both small and large MJO scales simultaneously, we can ask similar questions to the studies above, at least those related to relatively fast (over days or shorter) interactions between the large-scale environment and circulation and the convective scales. Although we are limited to a single 10-day case study on a large but limited-area domain, there is still some benefit to asking these kinds of questions of simulations in our novel framework. Hopefully these results will inspire other studies of the relationship between convective processes and large-scale phenomena, as well as ideas of further potential improvements to convective parameterizations in GCMs.

The paper layout is as follows. The model setup is briefly reviewed in section 2. Data and some methodological details are described in section 3. The main results are divided into moisture budget analysis (section 4), analysis of profiles of heating and vertical velocity (section 5), and moist entropy budget analysis (section 6). Finally, section 7 contains discussion and conclusions.

2. Model setup

The model setup is explained extensively in H13 and H12. Briefly, we use the limited-area mode of version 7.1 of MetUM (Davies et al. 2005), which is semi-Lagrangian and nonhydrostatic; our limited-area runs are updated at the lateral boundaries by ECMWF operational analyses. The initial conditions also come from an ECMWF forecast analysis (except for MetUM SST analysis, which is fixed at the initial value). The simulations all start at 0000 UTC 6 April 2009 and run for 10 days, part of MJO Case D of the Year of Tropical Convection (YOTC; Waliser et al. 2012). The 40- and 12-km-horizontal-grid model runs are updated directly from the ECMWF analyses every 6 h at the lateral boundaries via a rim of eight model grid points, within which the prognostic fields are blended linearly between the interior model domain and the exterior analysis. The 4-km grid runs are updated every 30 min from lateral boundary conditions computed from the 12-km param run. The 12-km domain is approximately 21°S–21°N, 41°E–178°W, the 4-km domain is set about 1° inside of this on all four sides, and the 40-km domain is similar to the 12-km domain, except that its eastern limit is about 3.5° farther west.

In addition to differences in horizontal grid spacing, there are more vertical levels in the 4-km runs (70 levels) than in the 12- and 40-km runs (38 levels), with the model top around 40 km high in both cases. Vertical spacing between levels ranges from tens of meters in the boundary layer to around 250 m in the free troposphere for the 4-km models and approximately double this for the 12- and 40-km models. The vertical levels are terrain-following hybrid heights.

The model physics settings differ between the runs as follows: the 12-km param model uses a modified Gregory–Rowntree convective parameterization [with convective available potential energy (CAPE) as the basis for its closure; Gregory and Rowntree 1990] with a 30-min CAPE relaxation time scale, as well as an adjustment to reduce this at very high vertical velocity in order to prevent gridpoint storms. The standard boundary layer scheme (Lock et al. 2000) is used for vertical subgrid mixing, and there is no horizontal subgrid mixing. There is a single-moment mixed-phase microphysics scheme with two components: ice/snow and liquid water (Wilson and Ballard 1999); rainfall is diagnosed at each time step, although reevaporation of rainfall is included. The 40-km param model is similar to the 12-km param model, but the convective parameterization has a CAPE relaxation time scale that is reduced at larger relative humidity, rather than at high vertical velocity.

The 4-km 3Dsmag model and 12-km 3Dsmag model use a CAPE-limited version of the convective parameterization (Roberts 2003; Lean et al. 2008) that asymptotically approaches the same 30-min CAPE time scale at zero CAPE but has a CAPE time scale that rapidly increases with increasing CAPE such that, for typical tropical values, virtually all rainfall is generated explicitly. These model versions do not use the standard boundary layer scheme for vertical subgrid mixing, but instead include Smagorinsky-type subgrid mixing in all three dimensions. The microphysics scheme now has prognostic rain in addition to the two components in the version above.

Two new simulations in the present paper are 12-km 1.5ent and 40-km 1.5ent. These are very similar to the 12-km param and 40-km param models, respectively, but they have values of mixing entrainment and mixing detrainment (for midlevel and deep convection) that are 1.5 times the values in those models. These simulations were inspired by Klingaman and Woolnough (2014), who found that global MetUM simulations showed improved MJO amplitude and propagation when this change was made to the convective parameterization.

The time step is 5 min for the 12-km param and both 40-km runs, 2.5 min for the 12-km 1.5ent run, 75 s for the 12-km 3Dsmag run, and 30 s for the 4-km 3Dsmag run.

3. Data and methods

ECMWF operational analyses, which are at approximately 25-km grid spacing in the tropics and archived for YOTC, are used as lateral boundary conditions for the limited-area model runs.

Daily mean area-averaged heating, vertical velocity, and temperature from the Tropical Ocean Global Atmosphere Coupled Ocean–Atmosphere Research Experiment intensive flux array (TOGA COARE IFA, version 2 data; CSU TOGA COARE 2002; Ciesielski et al. 2003) and the Dynamics of the MJO (DYNAMO) northern sounding array (NSA) and southern sounding array (SSA) (version

3b data; CSU DYNAMO 2014; Ciesielski et al. 2014; Johnson and Ciesielski 2013) are used for analyses of heating, vertical velocity, and vertical advective cooling variability shown in the supplemental material. The TOGA COARE data period is 1 November 1992–28 February 1993 and is provided at 6-hourly intervals for the IFA polygon, which is centered near 2°S, 155°E and is roughly 5° × 5°. The DYNAMO data period is 1 October–31 December 2011 and is provided at 3-hourly intervals. The DYNAMO NSA is roughly 0°–5°N, 73°–80°E, and the DYNAMO SSA is roughly 8°S–0°, 73°–80°E. Data are provided at 25-hPa vertical resolution and plotted against the time-period average heights of those pressure levels for each sounding array dataset. Vertical velocity for these datasets is calculated from pressure velocity using the hydrostatic approximation.

Most analysis methodology is explained in the appropriate results sections, but a few methods are explained in more detail here.

a. *Precipitation equivalent from diabatic heating*

The precipitation equivalent is calculated from the vertically integrated subgrid diabatic heating defined in H12 and H13 and discussed in section 5 below. This subgrid heating includes latent heating (from both parameterized and explicit convection) as well as subgrid mixing, but it does not include radiative heating. Because the vertically integrated heating rates were weighted by mass but saved in kelvins per day without the corresponding mass values, they were converted back to energy units using an assumption of 900 hPa of total tropospheric mass in hydrostatic balance. The precipitation equivalent is very similar to total precipitation but suffers less from a bias in the 4-km 3Dsmag model due to nonconservation of moisture, in which there is consistently about 8% more rainfall than that predicted by the other terms of the moisture budget, presumably because the advection scheme is creating spurious rainfall that does not contribute much to heating (although there is a small residual term in the moisture budget even using the precipitation equivalent). We therefore use this precipitation equivalent metric in one figure below to reduce model discrepancies in rainfall that are not energetically relevant, although we use actual precipitation in the figures that break down all components of the moisture budget.

b. *Large-scale advective terms in entropy budget*

We have calculated the advective terms of the entropy budget (section 6) on a 1° latitude–longitude grid instead of the original grid. This is because, when we calculated these terms on the original grid, we found a strong local effect in the explicit convection models, meaning that much of our advection was being contributed by the accumulation of small-scale advection by flow into, up through, and out of convective cells passing across small-scale gradients that were not representative of surrounding larger-scale or mean gradients. This led to horizontal terms that were far too large and positive (reducing moist entropy locally) and vertical terms that were correspondingly less positive (reducing entropy much less), although the total advection (the sum of horizontal and vertical) was not much different when calculated on the 1° grid versus the original grid. Wang et al. (2014) also used a larger spatial grid when calculating advective terms used in moisture and moist static energy budgets (including gross moist stability terms) for regional-model simulations of MJO cases.

4. Moisture budget

As discussed above, if the MJO is a moisture mode, moist entropy should increase to the east of the active region and decrease to the west. If this were the case, we would expect to see relatively more moistening to the east of active areas of convection in the 4-km 3Dsmag model than in the 12-km param model, since moisture differences contribute most of the moist entropy differences in the tropics. (For a related look at the moist entropy budget, see section 6). Figure 1 shows Hovmöller plots of moisture-related quantities averaged between 7.5°S and 7.5°N over the 10-day MJO case. Figures 1a–f show that precipitation equivalent (calculated using the vertically integrated subgrid diabatic heating, as discussed in section 3) and vertically integrated moisture convergence propagate eastward over the 10 days in the 4-km 3Dsmag model, whereas there is much less eastward propagation in the 12-km param model. All panels in Fig. 1 show line contours of vertically integrated subgrid diabatic heating (not including radiation) to aid in comparisons of other terms with this convective signal. This robust signal supports the conclusions of H13 that the 4-km 3Dsmag has much better MJO propagation (which is largely composed of an embedded eastward-propagating moist Kelvin wave during this time period, as mentioned in H13 and Waliser et al. 2012) than the 12-km param model (see comparison of these simulations with precipitation observations in Fig. 1 of H13), but this does not tell us about differences in moistening between the two models (since MC will mostly balance precipitation and/or heating).

To investigate the small imbalance that results in net moistening or drying by convection and advection, Figs. 1g–i show MC minus precipitation equivalent. This does not include evaporation, which is slightly higher in the 4-km 3Dsmag model (by 0.02 $\mathrm{mm\,h^{-1}}$ on average). The actual change in column water vapor (CWV) (the net moistening or drying by all processes) is shown in

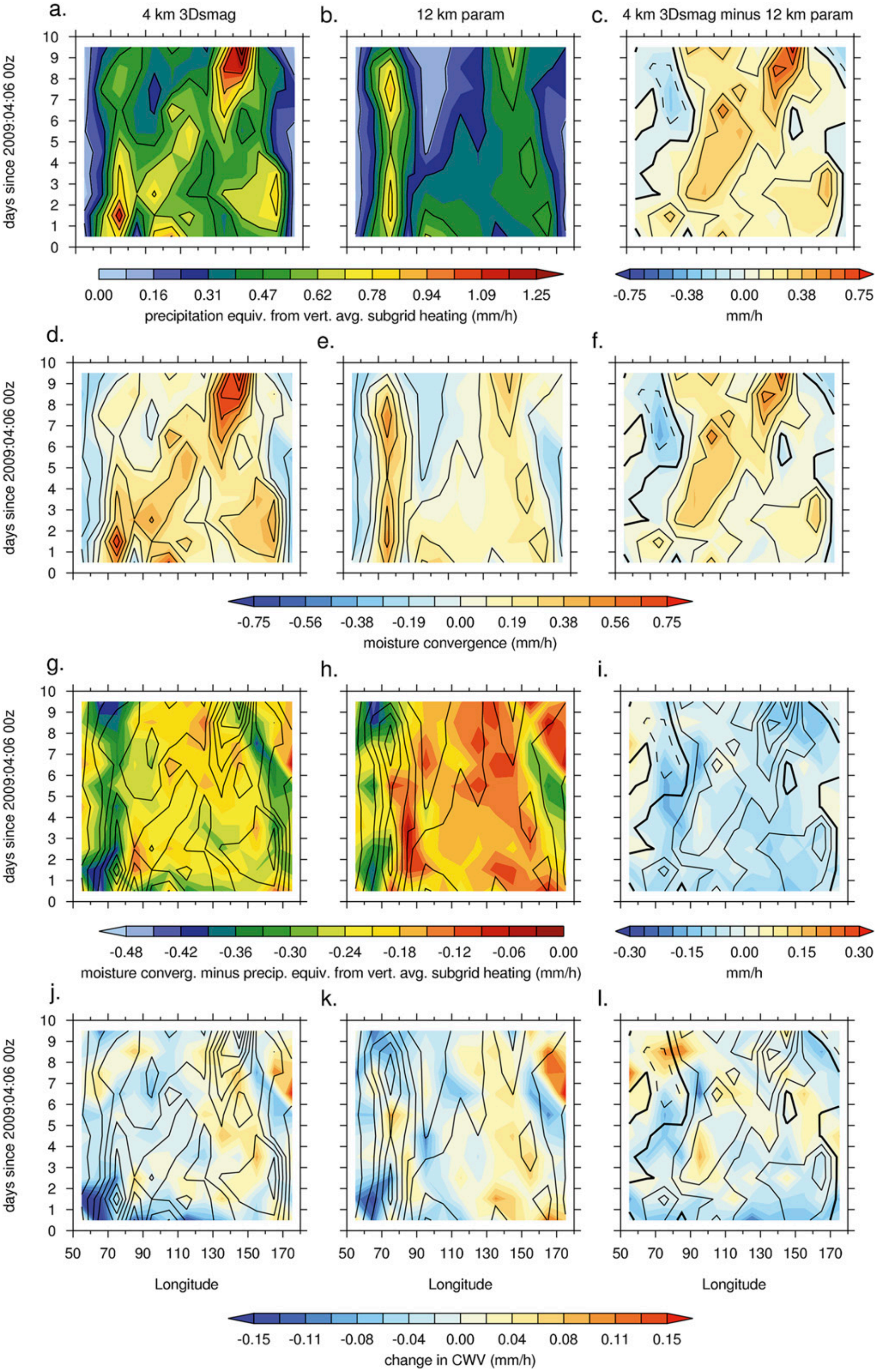

FIG. 1. Daily mean (a)–(c) precipitation equivalent calculated from vertically integrated subgrid heating, (d)–(f) MC, (g)–(i) MC minus this precipitation equivalent, and (j)–(l) change in column water vapor for (left) the 4-km 3Dsmag and (center) the 12-km param runs and for (right) their difference for 10° longitude boxes between 7.5°S and 7.5°N for the 10-day case study. Line contours of vertically averaged subgrid heating are overlaid, with a contour interval of 1 K day^{-1}, negative contours dashed, and zero contour thick.

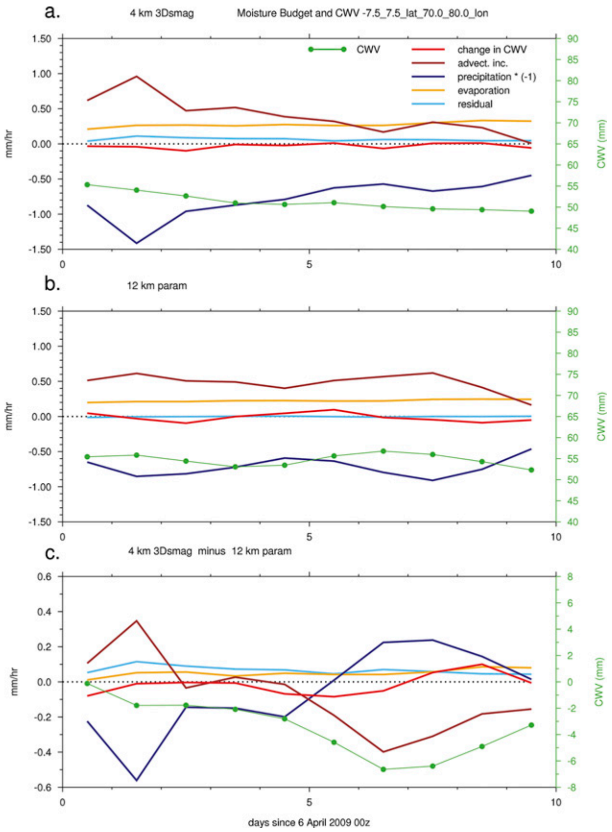

FIG. 2. Daily mean moisture budget terms (left axes) and total CWV (right axes), for (a) the 4-km 3Dsmag model, (b) the 12-km param model, and (c) their difference for a box covering 7.5°S–7.5°N, 70°–80°E for the 10-day case study. The total advective increment (advect. inc.) is the MC.

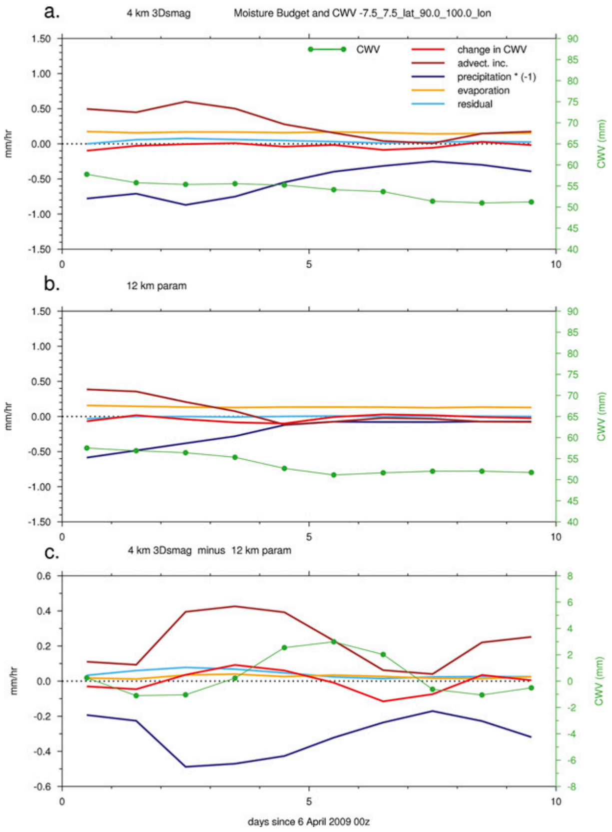

FIG. 3. Daily mean moisture budget terms (left axes) and total CWV (right axes), for (a) the 4-km 3Dsmag model, (b) the 12-km param model, and (c) their difference for a box covering 7.5°S–7.5°N, 90°–100°E for the 10-day case study. The total advective increment is the MC.

Figs. 1j–l. Even accounting for the slight difference in evaporation, there is still a bias (due to nonconservation, as discussed in section 3) evident in the 4-km 3Dsmag model, as shown by a larger net change in CWV in Figs. 1j–l than is implied by the MC minus precipitation equivalent in Figs. 1g–i. However, putting these issues to one side, there is evidence in Figs. 1g–h that the 4-km 3Dsmag model moistens slightly more in a band stretching from about 90°E in the early part of the period to about 110°E later on (relative to other regions and/or times in the same model) than the 12-km param model as a result of advective minus precipitation processes. This is seen as relatively less blue (or more yellow) color in Fig. 1i, ignoring the overall negative bias.

This difference in relative moistening is also somewhat evident in Figs. 1j–l. While there is not a coherent difference between the two models on the largest scales, with both models moistening overall in the eastern half of the domain (of order 1 mm day^{-1}) and drying in the western half, there are differences surrounding the main convective regions. Focusing on the 70°–80°E longitude band, the 4-km 3Dsmag model dries around days 4–7, whereas the 12-km param model moistens, perhaps contributing to the lack of eastward convective propagation in the 12-km param model, as discussed in H13. At 95°E, the 4-km 3Dsmag model has less of a CWV loss than the 12-km param model around days 4–5 and a greater loss to the west of that in days 4–6. Then the positive difference in CWV change for the 4-km 3Dsmag model moves eastward to around 110°E by days 6–8 and is replaced by a negative difference around 95°E. Although it is difficult to argue that the 4-km 3Dsmag drying at earlier times in the western regions causes the moistening farther east a little later (or vice versa), one proposed mechanism for eastward propagation of the MJO is the advection of drier air from off-equatorial regions or drier western equatorial regions by equatorially trapped Rossby waves moving west from the MJO active region (e.g., Maloney et al. 2010; Pritchard and Bretherton 2014).

The differences discussed above are illustrated further in Figs. 2 and 3, which show moisture budgets over the

10-day case study period for two equatorial boxes (note that actual precipitation, not precipitation equivalent, is shown in these figures). For instance, the transition to lower CWV in the 4-km 3Dsmag model at 70°–80°E, compared with relatively steady values in the 12-km param model, is evident in Fig. 2c, whereas the larger CWV in the 4-km 3Dsmag model at 90°–100°E relative to the 12 km param model in the middle of the period can be seen in Fig. 3c. This difference between the models is related around day 4.5 to larger precipitation in the 4-km 3Dsmag model and similar MC in both models and then is followed by a large relative decrease in MC in the 4-km 3Dsmag model over the next 2 days, which more than compensates for a relative decrease in precipitation.

Figures 2 and 3 show that the dominant terms in the moisture budget for both models are precipitation and MC and that changes in one of these terms are mostly offset by changes in the other. Furthermore, the interesting differences in CWV change between the two models are relatively small compared with both the main terms and with the overall larger-scale moistening in the eastern half of the domain in both models (perhaps indicating that horizontal advection from the imposed lateral boundary conditions is the main source of this moistening; cf. DeMott et al. 2014). It is difficult to tell whether these smaller signals in relative moistening between the models are important to their difference in MJO performance. This has been found by many previous studies of tropical convection and is one reason that studies often look at moist static energy or moist entropy instead of moisture budgets. Following moisture-mode thinking further, we will next look at vertical profiles of heating and vertical velocity before investigating moist entropy budgets.

5. Diabatic heating and vertical velocity profiles

To explore the relationships between convective heating, circulation, and the MJO in the 4-km 3Dsmag and 12-km param models, we define a subgrid heating term Q_C, not including radiation, as in Eq. (5) of H12 (except, in that paper, Q_C was labeled as Q_1):

$$\frac{1}{c_p}Q_C = \frac{L}{c_p}(c-e) - \frac{\Pi}{\overline{\rho}}\frac{\partial\overline{\rho w'\theta'}}{\partial z}, \tag{1}$$

where c_p is the specific heat capacity for dry air at constant pressure, L is the latent heat of condensation, c is condensation, e is evaporation of condensate (only liquid–vapor phase transitions are included in the equations for simplicity, although, in the model calculations, ice-phase transitions are also accounted for), θ is potential temperature, w is the vertical velocity, ρ is the density, z is height, Π is the Exner function defined as

$$\Pi = \left(\frac{\overline{p}}{p_0}\right)^{R/c_p},$$

R is the gas constant for dry air, p is the pressure, and $p_0 = 1000$ hPa is the reference pressure. We designate X' as the anomaly of quantity X from $\overline{X}$, which is the horizontal average of X at a single level and time over the large scale (1° in latitude and longitude in this case). As in H12 and H13, the first term on the rhs of Eq. (1) is calculated by adding the temperature increments directly output from the model schemes for convective parameterization, boundary layer/large-scale cloud (including vertical subgrid turbulence mixing and surface sensible heat flux), large-scale precipitation, and horizontal subgrid turbulence mixing (the latter is only applicable to the 4-km 3Dsmag model). The last term in Eq. (1) is a combination of temperature increments output from the advection scheme and subgrid vertical transport calculated on 3-hourly, 1° latitude–longitude boxes on model (hybrid height) levels, using the original model grid spacing (e.g., 4 km) to calculate X'. Values of Q_C are then coarse grained to 10° longitude, 7.5°S–7.5°N, and daily averages for the rest of the analyses. Note that Q_C and other heating rates are sometimes scaled by $1/c_p$ in figures.

Vertical averages of quantities are taken as mass-weighted averages between 0- and 18-km height. For averages of vertically averaged heating, for composites on vertically averaged heating bins, and for quantities normalized by vertically averaged heating, values that are on the 10° × 15°, 3-hourly grid that have vertically averaged heating below 0.65 K day^{-1} are set to missing before further averaging occurs.

We first investigate histograms of vertically averaged subgrid heating. The 12-km param model has a narrower distribution of daily mean vertically averaged heating, with a peak that is at a lower heating rate than the peak for the 4-km 3Dsmag model (Figs. 4a,b), relating to a preferred rain rate in the 12-km param model that results in too much light rain in general (see H12, which showed similar properties for 3-hourly 1° means).

By normalizing vertical profiles of heating by their vertical means and then compositing the normalized vertical profiles on vertically averaged heating in each of these bins, we can investigate the shapes of the heating profiles, since profiles that are more top-heavy would be expected to have a larger vertical component of NGMS and contribute to a reduction of moist entropy by the convective circulation. The preferred light-rain peak vertically averaged heating bin in the 12-km param model has a corresponding normalized heating profile

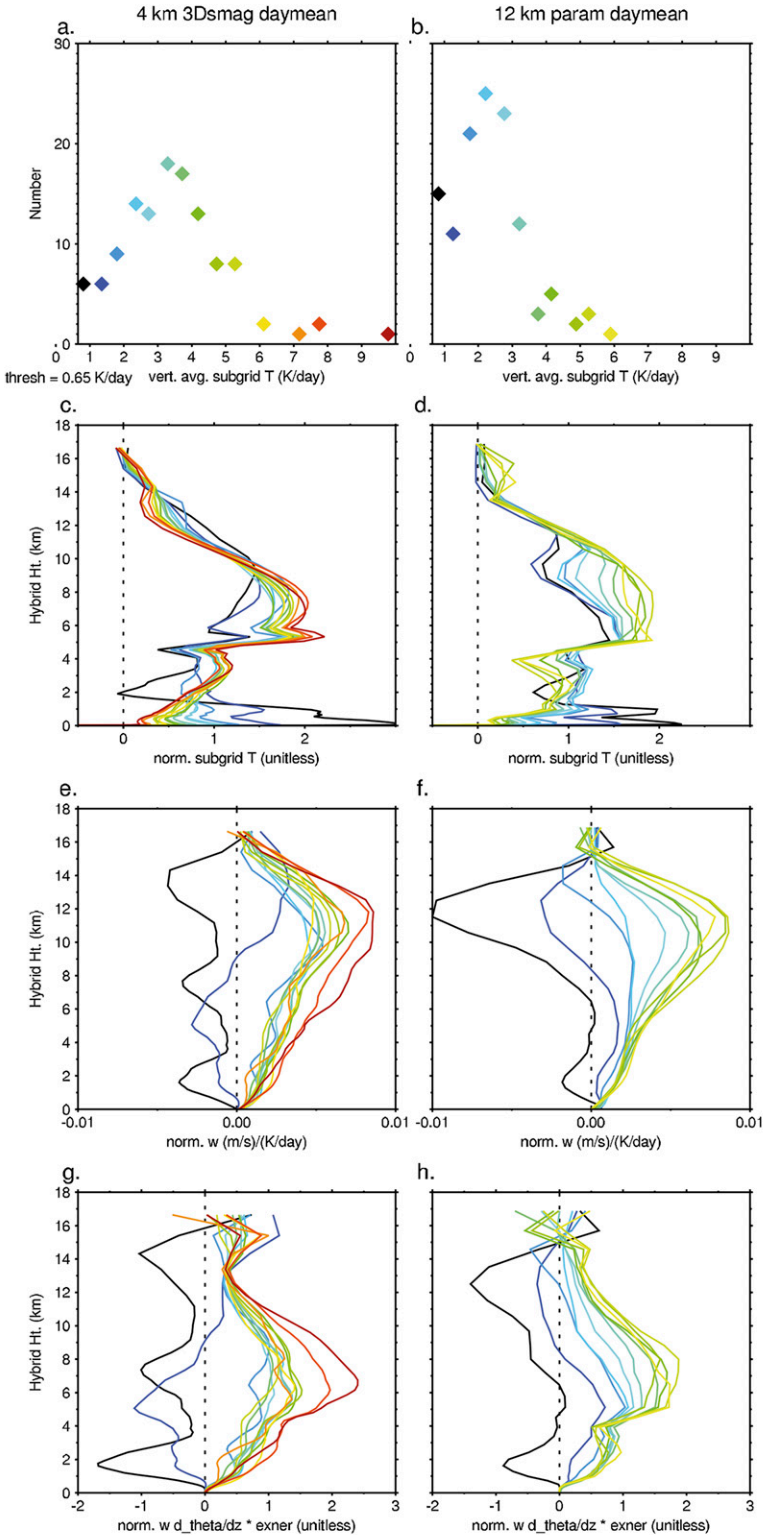

FIG. 4. (a),(b) Histograms of vertically averaged subgrid heating increments conditionally averaged by the column vertical average (0–18 km); (c),(d) vertical profiles of subgrid heating increments composited and normalized by these vertically averaged heating values; (e),(f) composited and normalized vertical velocity; (g),(h) as in (e) and (f), but multiplied by $\Pi\partial\theta/\partial z$ for (left) the 4-km 3Dsmag and (right) the 12-km param models for 10° longitude boxes covering 7.5°S–7.5°N and daily means for the 10-day case study.

(the light blue line in Fig. 4d) that is not very top-heavy and that has a fairly large increase in normalized heating rate between 0- and 4-km height, which may mean that this level of convection is relatively self-sustaining and stable from an MC and circulation perspective. In general, the 4-km 3Dsmag model has a more top-heavy overall tropospheric heating shape that is more consistent across different vertically averaged heating bins than the 12-km param model (Figs. 4c,d). Indeed, section 6 below shows that the vertical component of NGMS is lower, in general, for the 12-km param model relative to the 4-km 3Dsmag model. The 12-km param model is less top-heavy in its most frequently occurring bins, while the infrequent, stronger convection bins have significantly more normalized upper-level heating and less lower-level heating, making them much more top-heavy. Thus, the convection in the 12-km param model may be constrained toward its equilibrium over many regions, making it more difficult to transition to stronger or weaker rainfall in any one region. This also would presumably make it difficult for an active area of rainfall in one region to propagate to a new region. Note that standard deviations of these composite profiles (not shown) are generally less than 0.5, except for the smallest bin, which has values up to 0.8 at a few levels for each model.

The mean MC increases linearly with vertically averaged subgrid heating in both models (not shown), which is expected, since vertically averaged subgrid heating should be mainly balanced by MC and evaporation; the 12-km param model has slightly higher values of MC in most bins (typically 0.04 mm h^{-1} higher, and about 0.08 mm h^{-1} higher in the two bins between 1 and 2 K day^{-1} and the bin around 3.75 K day^{-1}). Figures 4c and 4d show that, in the 4-km 3Dsmag model, larger vertically averaged heating (warmer bin color) corresponds to more heating between 2- and 4-km height relative to the heating between 0- and 2-km height than in the 12-km param model, which one might think would allow for more low-level convergence and, therefore, more MC per upper-level divergence, yielding a lower vertical component of NGMS. This difference in the shape of low-level heating is discussed below, along with its possible relevance to MJO performance, while NGMS components are analyzed in section 6.

On large scales, vertical advection largely balances diabatic heating in the tropics, meaning that there are strong relationships between diabatic heating profiles and vertical velocity profiles. In Fig. 4f, the lower-tropospheric vertical velocity (normalized by vertically averaged heating) in the 12-km param model is very similar for all average heating rates except the two lowest bins. It is only the shape of the profile above about 5-km height that changes much, increasing with vertically averaged heating. This means that there is more overall upward vertical velocity per vertically averaged heating at higher average heating rates. It also suggests that the high-heating-rate bins (which, again, are infrequent for this model) have significantly more divergence of moist entropy aloft per vertically averaged heating (and MC), meaning a higher vertical component of NGMS (however, the profile of moist entropy also plays a role, as discussed in section 6 below). In the 4-km 3Dsmag model (Fig. 4e), most bins have a similar shape to each other, and this shape is more top-heavy than the most populous 12-km param bin shapes but less top-heavy than the 12-km param high-heating-rate bin shapes. Note that standard deviations of these vertical velocity composites (not shown) are typically 0.001–0.003 m s^{-1} (K day^{-1})$^{-1}$ for most bins, but they are significantly larger at lower-tropospheric levels for the 4-km 3Dsmag than the 12-km param model, while they are similar for the models at higher levels. For all but the three lowest bins, the standard deviations for both models peak around 0.0025 m s^{-1} (K day^{-1})$^{-1}$.

Figures 4g and 4h show the estimated net cooling effect of the normalized vertical velocity profiles, $\langle w\rangle\langle\Pi\rangle\partial\langle\theta\rangle/\partial z$, where w is the normalized vertical velocity, and $\langle X\rangle$ in this case is the average of quantity X for daily means over the 10° × 15° boxes and each vertically averaged heating bin. These look more like the heating profiles than the normalized vertical velocity profiles alone, especially for the 12-km param model, which shows a very smooth progression at upper levels toward larger adiabatic cooling for larger vertically averaged heating bins. The 4-km 3Dsmag model has more variability than the 12-km param model; when broken down into 3-hourly data (not shown), it also has more vertical degrees of freedom than the 12-km param model, meaning the shapes of the profiles, not just the amplitudes, are more variable during different times of day in the 4-km 3Dsmag model. The vertical integrals of the estimated cooling profiles in Figs. 4g and 4h relate to the export of dry entropy by the mean vertical velocity normalized by vertically averaged subgrid heating. Overall, these estimated cooling profiles in Figs. 4g and 4h, which better estimate the amount of export of upper-tropospheric dry entropy per vertically averaged heating than the w profiles alone, tell a similar story in comparing the two models as that told above in the discussion of the w profiles: most 4-km 3Dsmag model bins are very similar to each other, and the amount of total normalized estimated cooling (the mass-weighted vertical integral) for most of these bins is more than the amounts for the most populous (light blue) 12-km param bin profiles but somewhat smaller or roughly similar to the amounts for the 12-km param high heating rate profiles.

The analyses shown in Fig. 4 have also been done for the 40-km param, 12-km 3Dsmag, 40-km 1.5ent, and 12-km 1.5ent simulations. The 1.5ent models (with increased entrainment, as described in section 2 above) have better MJO amplitude and propagation than the 12-km param and 40-km param models, particularly in principal component analysis (see H13) based on Wheeler and Hendon (2004) and energetics terms (see Figs. S1–S4 in the supplemental material). The normalized subgrid heating profile shapes for the 40-km param model are similar to those of the 12-km param model, while the 12-km 3Dsmag model is similar to the 4-km 3Dsmag model (see Fig. S5). The two 1.5ent models are somewhere in between the explicit convection simulations and the param simulations (see Fig. S6), with patterns of top-heaviness over the whole troposphere more similar to the param models, but with changes in the lower troposphere (0–4 km) being somewhat more similar to the explicit convection models, in that the normalized heating tends to increase with height through most of the lower troposphere for most heating bins.

To evaluate our assumption that the explicit convection simulations have more realistic vertical heating, velocity, and advective cooling structures, we have also done similar analyses using daily mean domain-averaged data from TOGA COARE and the DYNAMO NSA and SSA (see Fig. S7). Because the diabatic heating for these observations Q_1 includes radiative heating, we have also recalculated the analyses for each model using Q_1, where $Q_1 = Q_C + Q_R$ and Q_R is the total radiative heating (Figs. S8–S10). The observations (though from different time periods and much fewer spatial locations than the model output) confirm that the explicit convection simulations are more realistic, with fairly similar shapes for different heating rates and heating rates that increase smoothly upward in the lower troposphere.

To look further into the effects of different shapes of lower-level heating, Figs. 5a and 5b show Hovmöller plots of the difference between the normalized subgrid heating profiles averaged between 2- and 4-km height and those averaged between 0- and 2-km height for daily means of both models (these vertically averaged layers are not weighted by mass). The idea behind this analysis is to estimate the degree to which heating increases upward in the lower troposphere and thereby potentially leads to more low-level convergence, which could be important for NGMS or for other dynamical processes. In the 4-km 3Dsmag model, this quantity is fairly large in areas with large total vertically averaged subgrid heating, as expected from Fig. 4c. The 12-km param model does not have this relationship, largely because of cooling from melting and evaporation of falling hydrometeors in the large-scale precipitation scheme between 2- and 5-km height at higher rain rates, which, while smaller than comparable cooling in the 4-km 3Dsmag model, is not balanced by extra heating from the convection scheme, whereas the 4-km 3Dsmag model has large-scale cloud heating that compensates the melting and evaporative cooling (not shown). Chikira (2014) argues that cooling from melting and evaporation of hydrometeors in the lower troposphere act as a net drying on the column because decreased vertical moisture advection wins out over moistening by evaporation; they also find that the melting of snow occurs much more

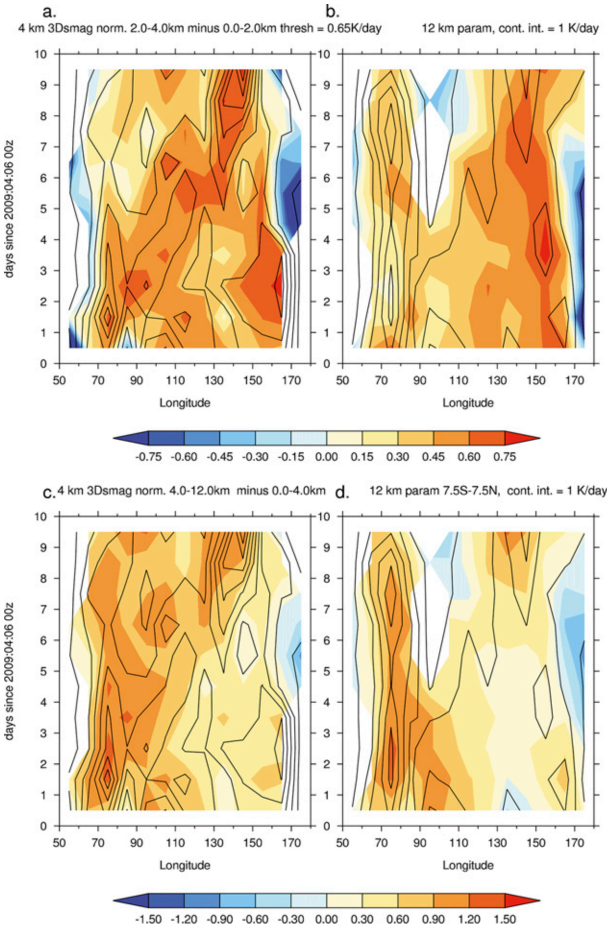

FIG. 5. Hovmöller plots of the difference between layers of vertically averaged normalized subgrid heating for (a),(b) 2–4-km height minus 0–2-km height and (c),(d) 4–12-km height minus 0–4-km height (with values taken as missing where the vertically averaged subgrid heating is below 0.65 K day^{-1}), along with line contours of vertically averaged subgrid heating (with a contour interval of 2 K day^{-1}) for (left) the 4-km 3Dsmag and (right) the 12-km param runs on daily mean time scales for 10° longitude boxes covering 7.5°S–7.5°N for the 10-day case study.

for more top-heavy profiles. Again, it may be important that this cooling term is balanced by cloud latent heating in the 4-km 3Dsmag model but not in the 12-km param model.

The 4-km 3Dsmag model pattern for this lower-tropospheric heating metric also looks similar to its pattern of rainfall and MC, which, again, makes sense if it corresponds with large subgrid heating. However, this metric does more than simply correlate with total heating: note that the high values for the 4-km 3Dsmag model largely follow the main eastward-propagating Kelvin wave embedded within the MJO envelope, staying fairly high and constant even during fluctuations in actual heating rates (Fig. 5a). So it appears that the convectively active MJO region has disproportionately high values of this metric for this model. For the 12-km param model (Fig. 5b), this metric seems to be mainly related to longitude, with higher values being present in the eastern part of the domain (roughly 130°–160°E) for the entire period (where melting and evaporative cooling from the large-scale precipitation scheme is generally small; not shown).

The MJO signal for the 4-km 3Dsmag model is less clear for the difference in average normalized vertical velocity for 2–4-km height minus 0–2-km height in Fig. 6a. This suggests that any physical mechanism connecting the increase in normalized lower-tropospheric heating with height to the MJO is more complex than simply a similar increase in lower-tropospheric vertical velocity leading to more low-level convergence. Possibilities include differences in stability for boundary layer parcels or the effects of cold pools generated by evaporation of hydrometeors, but testing these further is beyond the scope of this paper.

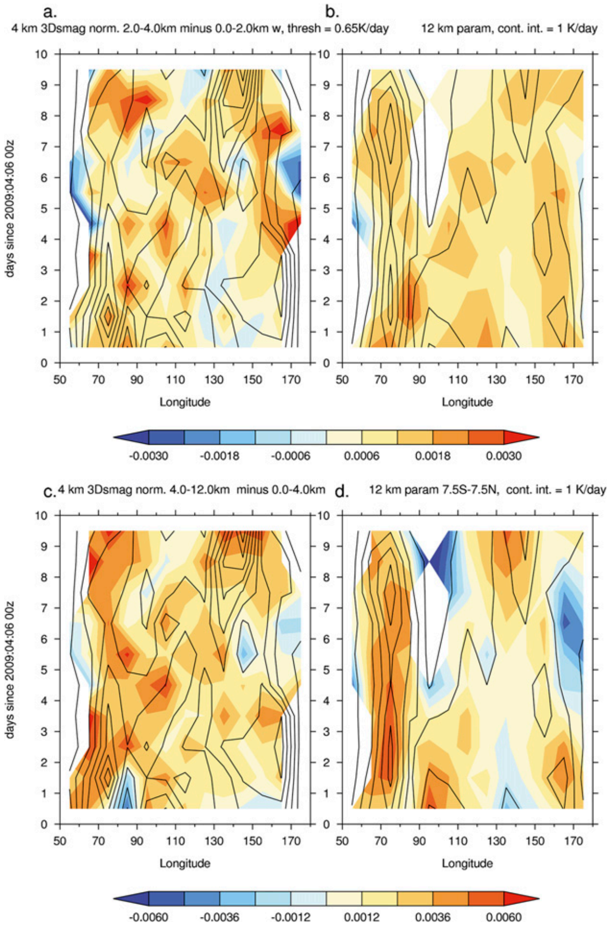

FIG. 6. Hovmöller plots of the difference between layers of vertically averaged normalized vertical velocity for (a),(b) 2–4-km height minus 0–2-km height and (c),(d) 4–12 km height minus 0–4-km height (with values taken as missing where the vertically averaged subgrid heating is below 0.65 K day^{-1}), along with line contours of vertically averaged subgrid heating (with a contour interval of 2 K day^{-1}) for (left) the 4-km 3Dsmag and (right) the 12-km param runs on daily mean time scales for 10° longitude boxes covering 7.5°S–7.5°N for the 10-day case study.

A similar metric to those mentioned above, but measuring overall tropospheric top-heaviness of heating rather than lower-tropospheric increase in heating with height, is the difference in average normalized subgrid heating (or normalized vertical velocity) for 4–12-km height minus 0–4-km height. These are shown as Hovmöller plots in Figs. 5c and 5d and Figs. 6c and 6d. For the heating in Figs. 5c and 5d, the 4-km 3Dsmag model is clearly more top-heavy at and behind the moist Kelvin wave than in front of it. The 12-km param model begins the period with a similar distribution of top-heavy heating as the 4-km 3Dsmag model (larger in the western half of the domain), but this region shrinks within the first few days to cover mainly the 60°–80°E band of strong convection, and it also decreases slightly in amplitude. Vertical velocity top-heaviness in Figs. 6c–d is somewhat noisier but shows a generally similar picture to the heating for both models. Overall, for both heating and vertical velocity, the 12-km param model tends to have top-heaviness that correlates fairly well on daily time scales to vertically averaged heating, whereas the 4-km 3Dsmag model shows more variation of top-heaviness within contours of vertically averaged heating and more relationship between top-heaviness and MJO (or Kelvin wave) phase. This evidence lends some extra support to the conjecture above that the way the shapes of the heating profiles depend on the total heating may make it more difficult for the 12-km param model to reduce strong convection at and behind the active regions and transition to new convective regions than for the 4-km 3Dsmag model to do so, since convection seems to have the same amount of top-heaviness for a given total

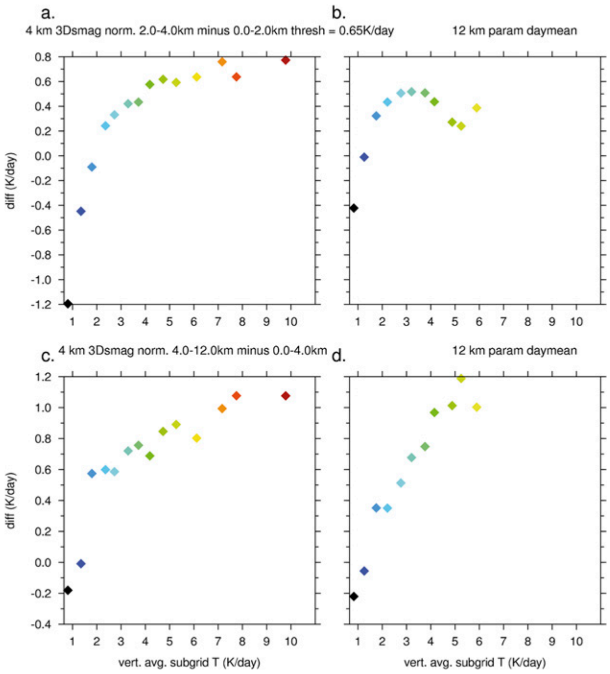

FIG. 7. Difference between layers of vertically averaged normalized subgrid heating for (a),(b) 2–4-km height minus 0–2-km height and (c),(d) 4–12-km height minus 0–4-km height (with values taken as missing where the vertically averaged subgrid heating is below 0.65 K day^{-1}), conditionally averaged in bins of vertically averaged subgrid heating for (left) the 4-km 3Dsmag and (right) the 12-km param runs on daily mean time scales for 10° longitude boxes covering 7.5°S–7.5°N for the 10-day case study.

heating rate no matter where it occurs in MJO phase and since top-heaviness is small for the most commonly occurring heating rates.

Figure 7 shows the subgrid heating top-heaviness metrics for the two models conditionally averaged in bins of vertically averaged subgrid heating. For the lower-tropospheric top-heaviness (Figs. 7a,b), the 4-km 3Dsmag model has a sharp increase in this metric, with increasing vertically averaged heating for low heating rates and then a slower increase at higher heating rates, while the 12-km param model actually has decreases in this metric above the 3 K day^{-1} vertically averaged heating rate, as was inferred from Fig. 4 in the discussion above. Also agreeing with the discussion above, while both models show an increase in the deep-tropospheric top-heaviness metric with vertically averaged subgrid heating, this increase is much steeper for the 12-km param model above 2 K day^{-1}, meaning that there is a larger disparity in tropospheric top-heaviness between the most common average heating and the largest average heating values for this model.

Comparing the two different top-heaviness metrics from Figs. 5–7 for each model, the 4-km 3Dsmag model has, overall, more similarities between the two metrics, although the deep-tropospheric top-heaviness is more pronounced at and behind the main Kelvin wave signal. The 12-km param model has, in many respects, a negative correlation between deep-tropospheric top-heaviness and lower-tropospheric top-heaviness. This agrees with impressions from Fig. 4 that the 4-km 3Dsmag has a single heating profile shape for moderate-to-heavy convection, whereas the 12-km param model has large changes in heating profile shapes for different amounts of total convective heating.

The top-heaviness metrics for the four other models broadly confirm the idea that the lower-tropospheric top-heaviness is higher (for larger heating bins) in the models with good MJO performance (see Figs. S11 and S12 in the supplemental material). These models also have lower-tropospheric top-heaviness more similar to observations (when compared using Q_1, see Figs. S13–S16).

6. Moist entropy budget

The moist entropy budget (or, similarly, the moist static energy budget) has been used by several studies to analyze or model the MJO (e.g., Sobel and Maloney 2012; Benedict et al. 2014). Moist entropy should be nearly conserved for moist adiabatic processes, leaving advective terms and three source terms (surface latent and sensible heat fluxes and atmospheric radiative fluxes) in the vertically integrated budget. The advective terms can be further broken down into vertical and horizontal components.

The moist entropy s is defined following Raymond (2013) and Benedict et al. (2014):

$$s = (c_p + r_V c_{pV}) \ln(T/T_R) - R \ln(p_D/p_0) - r_V R_V \ln(p_V/e_{\mathrm{SF}}) + (L_V r_V / T_R), \qquad (2)$$

where r_V is the water vapor mixing ratio, c_{pV} is the specific heat of water vapor, T is air temperature, $T_R = 273.1$ K, p_D is the partial pressure of dry air, R_V is the gas constant for water vapor, p_V is the partial pressure of water vapor, $e_{\mathrm{SF}} = 611$ Pa, and the latent heat of vaporization $L_V(T) \approx 2.5 \times 10^6$ J kg^{-1}. We neglect liquid and ice contributions as in Benedict et al. (2014). Following Raymond and Fuchs (2009) and Benedict et al. (2014), but using height coordinates and fields averaged onto our 1° grid (see section 3 above), the total (Γ_T), horizontal (Γ_H), and vertical (Γ_V) components of NGMS can be defined as follows:

$$\Gamma_T = -\frac{T_R[\rho\bar{\mathbf{v}}\cdot\nabla\bar{s} + \rho\bar{w}(\partial\bar{s}/\partial z)]}{L[\nabla\cdot(\rho r_V\mathbf{v})]}, \tag{3}$$

$$\Gamma_H = -\frac{T_R[\rho\bar{\mathbf{v}}\cdot\nabla\bar{s}]}{L[\nabla\cdot(\rho r_V\mathbf{v})]}, \quad \text{and} \tag{4}$$

$$\Gamma_V = -\frac{T_R[\rho\bar{w}(\partial\bar{s}/\partial z)]}{L[\nabla\cdot(\rho r_V\mathbf{v})]}, \tag{5}$$

where $[X] = \int_0^{z_1} X\,dz$, $z_1 \approx 20\,\mathrm{km}$, ρ is the density, $\mathbf{v}$ is the horizontal vector wind, and $\mathrm{MC} = -L[\nabla\cdot(\rho r_V\mathbf{v})]$ is calculated from advective increments of moisture directly output by the model (note that MC was scaled by $1/L$ in previous figures). The vertical component Γ_V is the quantity above that is most related to the original GMS first defined in Neelin and Held (1987).

The budget of $\bar{s}$ can be written:

$$T_R[\partial\bar{s}/\partial t] = -T_R[\rho\bar{\mathbf{v}}\cdot\nabla\bar{s}] - T_R[\rho\bar{w}(\partial\bar{s}/\partial z)] + \mathrm{LH} + \mathrm{SH} + [\mathrm{LW}] + [\mathrm{SW}] + \mathrm{Res}, \tag{6}$$

where LH and SH are the latent and sensible surface heat fluxes, respectively, LW and SW are the net longwave and shortwave heating, and Res is the residual when all the other terms on the rhs are subtracted from the lhs. For ease of reference later on, we also define the following normalized entropy divergence variables, analogous to the NGMS terms: $\Gamma_{\bar{s}_t} = T_R[\partial\bar{s}/\partial t]/\mathrm{MC}$, $\Gamma_{\mathrm{SF}} = -(\mathrm{LH} + \mathrm{SH})/\mathrm{MC}$, and $\Gamma_R = -([\mathrm{LW}] + [\mathrm{SW}])/\mathrm{MC}$. The residual can be significant for some regions and times, especially in the 4-km 3Dsmag and 12-km 3Dsmag models, although it is generally much smaller in amplitude than the other main rhs terms. The residual will reflect imbalances in the moist entropy budget due to neglected physical processes (such as ice–liquid phase changes, frictional dissipation, and irreversible diffusion of water vapor) and nonconservation in the model (related to numerical dissipation and other model inaccuracies).

Our use of 1° fields for advection calculations does not appear to affect the total advection very much, as noted in section 3 above, so this should not be a significant contribution to the residual. In Eq. (6), we have ignored the flux out of the top of the domain $\overline{ws}_{z_1}$, because it is fairly small and does not tend to make a systematic difference in either our conclusions or the size of the residual. In our analyses below, we use 10° × 15° averages containing only sea points, which are defined as 1° grid boxes containing, at most, 10% land using the 4-km model land mask.

Hovmöller plots of $\bar{s}$, $T_R[\partial\bar{s}/\partial t]$, Γ_V, Γ_H, and Γ_T are shown in Fig. 8 for the 4-km 3Dsmag model, the 12-km param model, and their difference, with contours of moisture convergence overlaid. Both models develop large $\bar{s}$ in the eastern half of the domain by the end of the period (Figs. 8a,b), as expected from the increases in CWV shown in Figs. 1j and 1k, but there are also some key differences between the models. Figure 8c shows comparatively larger entropy in the 90°–100°E band in the 4-km 3Dsmag model and, after day 5, less at 70°–80°E, supporting discussion of key moisture budget differences in section 4. The 4-km 3Dsmag model has larger $\bar{s}$ in the far eastern part of the domain as well. In Figs. 8d–f, $\partial\bar{s}/\partial t$ looks fairly similar to the change in CWV shown in Fig. 1 above (although the analysis in that figure used all points, not just sea points). It is hard to see patterns in Γ_V (Figs. 8g–i) beyond the generally larger values in the 4-km 3Dsmag model, although, admittedly, there are slightly lower values for the 12-km param model in the eastern half of the domain (relative to values in the western half for the same model), which might slightly aid eastward propagation in that model; these make sense given the generally lower values of tropospheric top-heaviness for vertical velocity in Fig. 6d. In Fig. 8l, Γ_H has a more pronounced negative difference in the east (larger values for the 4-km 3Dsmag model). For total NGMS (Fig. 8o), there are larger values to the west and middle of the domain and smaller values in the east overall for the 4-km 3Dsmag model, suggesting an overall large-scale difference favoring eastward propagation. It is also worth noting that Γ_H is the dominant component of Γ_T in the 12-km param model, whereas the two components are both important in the 4-km 3Dsmag model. The model differences in the various NGMS terms in Fig. 8 do not obviously explain the differences in MJO performance.

An example of the moist entropy budget, as well as the evolution of MC, is shown in Fig. 9 for 10°S–10°N, 70°–80°E. This can be compared with the moisture budget for this region in Fig. 2 (although, as mentioned, the moist entropy budget is only for sea points). Again, total entropy change (and total CWV change) is lower, and CWV and MC decline more, between days 4 and 7 in the 4-km 3Dsmag model relative to the 12-km param model, reflecting an eastward propagation of convective activity away from this region during that time. The lower-entropy-change term for the 4-km 3Dsmag model, which leads to significantly lower total entropy values at the end of day 6 (not shown), occurs because of significantly more negative vertical advective terms, as well as somewhat lower horizontal advective terms and slightly more net radiative cooling. These terms together are large enough to more than compensate for larger surface flux and residual terms. The 4-km 3Dsmag model also has significantly larger Γ_V and Γ_T, representing more export of moist entropy per MC for this model and region (Fig. 10). These larger NGMS values begin around day 2, preceding the differences in actual

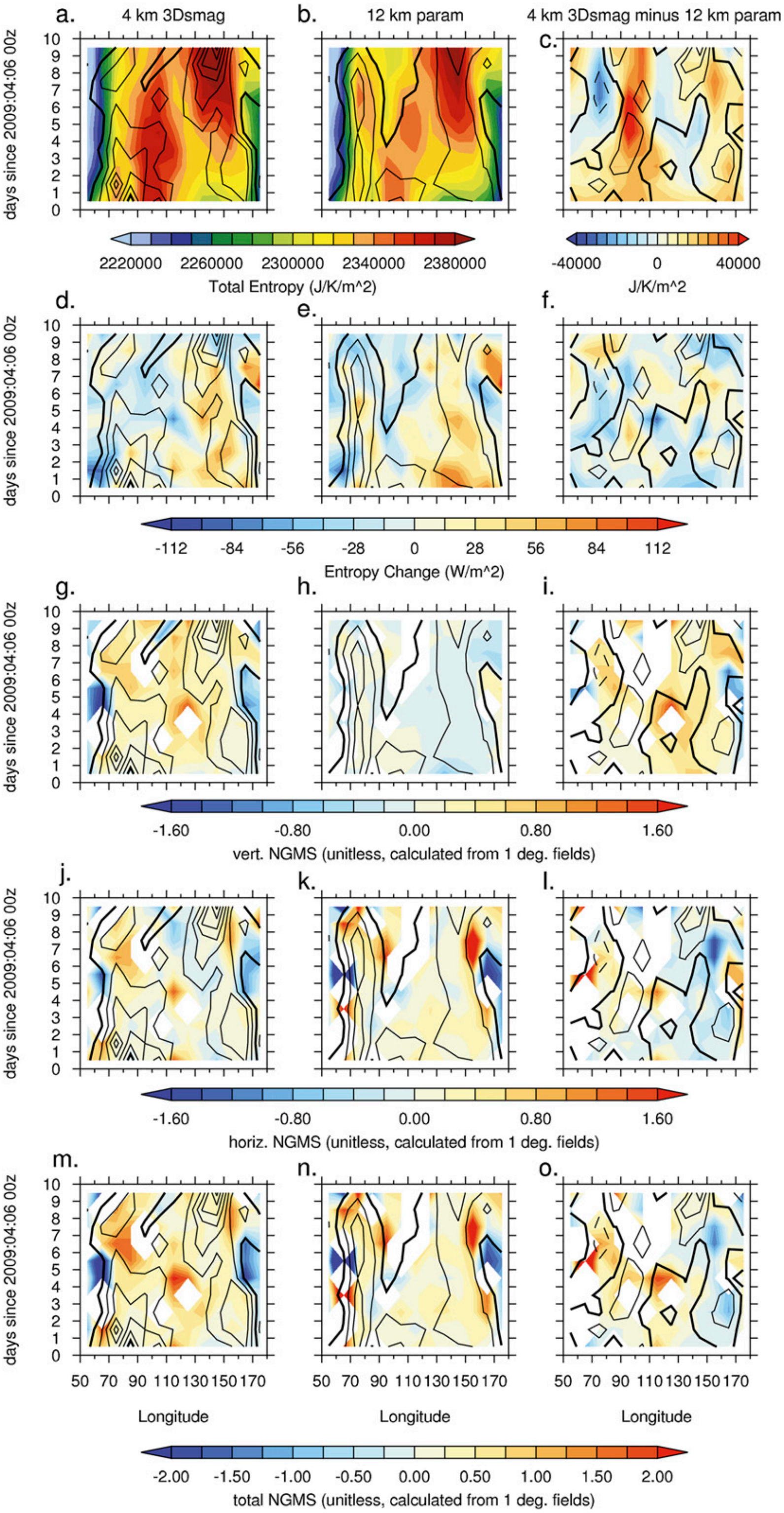

FIG. 8. Daily mean values over sea of (a)–(c) entropy, (d)–(f) entropy change ($\times T_R$), (g)–(i) vertical component of NGMS, (j)–(l) horizontal component of NGMS, and (m)–(o) total NGMS for (left) the 4-km 3Dsmag and (center) the 12-km param runs and for (right) their difference for 10° longitude boxes covering 7.5°S–7.5°N for the 10-day case study. Contour lines are moisture convergence with a thick zero line and dashed negative contours; contour spacing is 150 W m^{-2}. NGMS advection terms are calculated from fields averaged on a 1° grid.

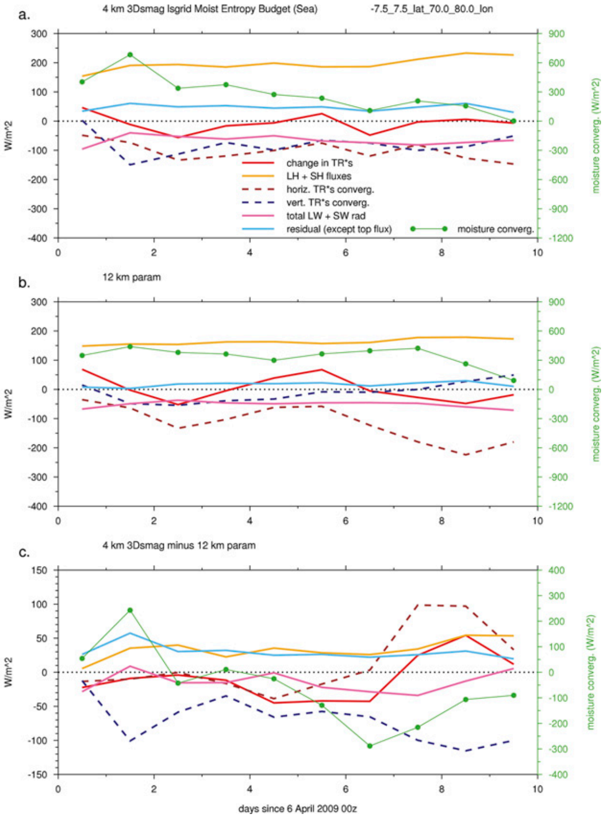

FIG. 9. Daily mean moist entropy ($\times T_R$) budget terms and total MC for (a) the 4-km 3Dsmag model, (b) the 12-km param model, and (c) their difference for a box covering 7.5°S–7.5°N, 70°–80°E for the 10-day case study. The advective terms have been calculated using fields averaged onto a 1° grid.

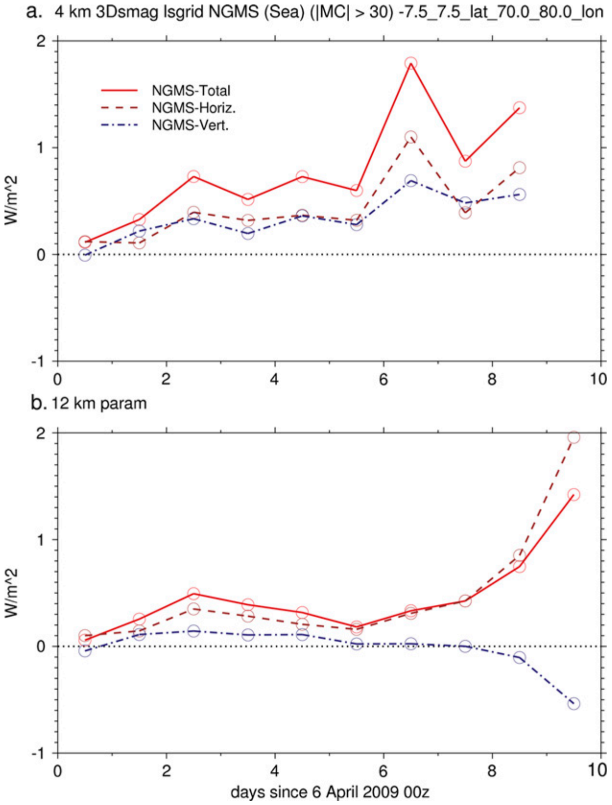

FIG. 10. Daily mean total, horizontal, and vertical NGMS for (a) 4-km 3Dsmag and (b) 12-km param runs, for a box covering 7.5°S–7.5°N, 70°–80°E for the 10-day case study. The advective terms have been calculated using fields averaged onto a 1° grid, and times with MC magnitudes below 30 W m^{-2} are not included.

entropy change that begin around day 4, so they could plausibly be causing these eventual differences in total entropy, which accompany the reduction in convection and MC in the 4-km 3Dsmag model in the middle of the period.

To get a sense of the moist entropy budget and NGMS across the whole equatorial domain, Figs. 11 and 12 show these terms across all equatorial boxes averaged on 10 April 2009, about halfway through the 10-day case study period for the 4-km 3Dsmag and 12-km param models. The 4-km 3Dsmag model has a mostly positive change in total entropy east of 130°E, with relatively small positive NGMS values there (and some negative NGMS far to the east, where there is small negative MC). In the 12-km param model, although there are also positive changes in total entropy between 130° and 160°E, the magnitude of this $T_R[\partial\overline{s}/\partial t]$ term is smaller over other longitudes, and there is still a small but significant positive entropy change between 70° and 80°E, reinforcing this model's behavior of maintaining convection where it was initialized in the central Indian Ocean, as described above. The 12-km param model also has much smaller NGMS terms at nearly all longitudes at this time, whereas the total NGMS for the 4-km 3Dsmag (outside areas of negative MC) is generally higher near and to the west of the peak convective region (75°–130°E) compared with the eastern area (135°–155°E), contributing to lower $T_R[\partial\overline{s}/\partial t]$ terms to the west and therefore aiding the eastward propagation of the MJO. Sobel et al. (2014) and Wang et al. (2014) show similar increases in advective export terms and NGMS ahead of the active regions of the MJO in DYNAMO NSA observations and regional explicit convection simulations of the DYNAMO period, respectively. Values of NGMS for the 4-km 3Dsmag model are generally larger, with larger variance among different longitudes, than values in the 12-km param model. These results hold broadly true for the 12-km 3Dsmag model versus the 40-km param model as well (not shown).

The lower values of Γ_V for the 12-km param and 40-km param models, even for higher vertically averaged heating rates that have top-heavy heating profiles, appear to be a result of lower $\partial s/\partial z$ from around 1- to 4-km

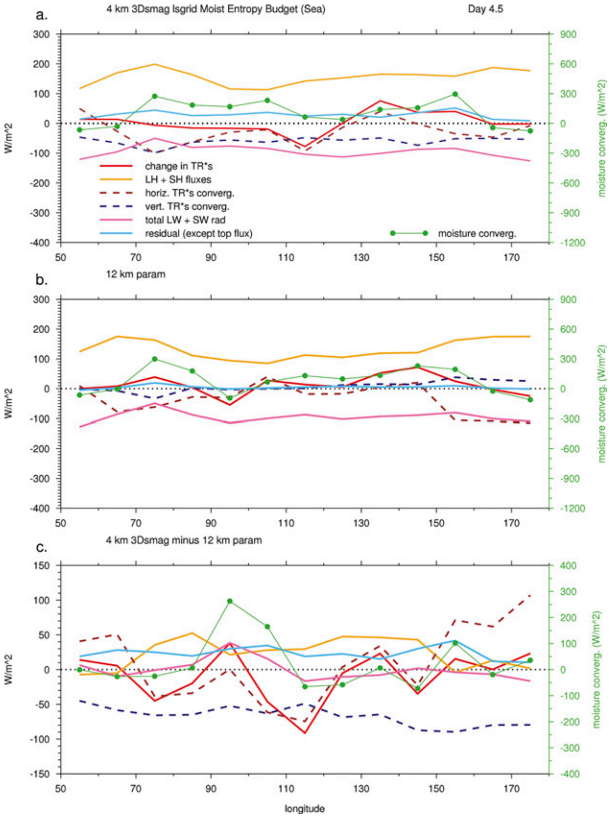

FIG. 11. Daily mean moist entropy ($\times T_R$) budget terms and total MC for (a) the 4-km 3Dsmag model, (b) the 12-km param model, and (c) their difference, averaged in boxes 10° longitude across and covering 7.5°S–7.5°N for 10 Apr 2009. The advective terms have been calculated using fields averaged onto a 1° grid.

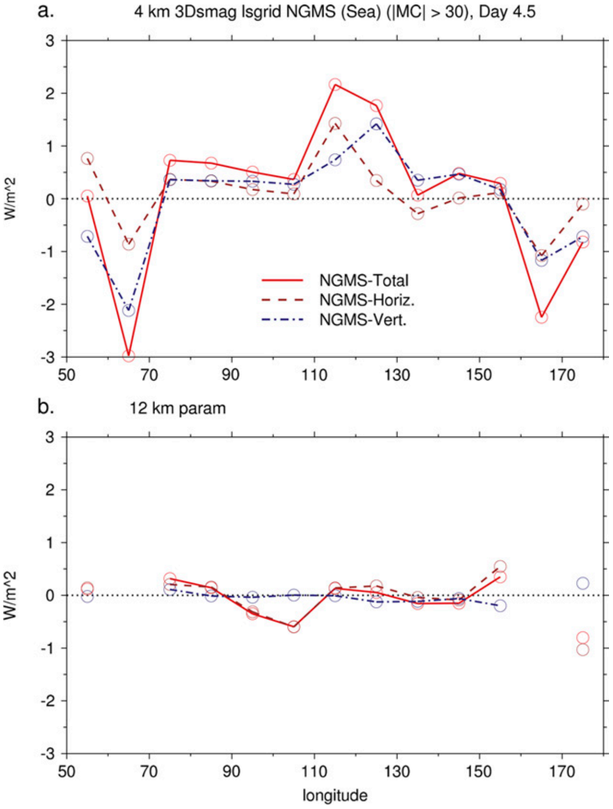

FIG. 12. Total, horizontal, and vertical NGMS for (a) 4-km 3Dsmag and (b) 12-km param runs, averaged in boxes 10° longitude across and covering 7.5°S–7.5°N for 10 Apr 2009. The advective terms have been calculated using fields averaged onto a 1° grid, and times with MC magnitudes below 30 W m^{-2} are not included.

height in these models. This is related mostly to lower $\partial\theta/\partial z$ at those levels, as can be inferred from Figs. 4g and 4h (and Figs. S5g,h). The parameterized convection models also have a more negative $\partial q/\partial z$ around 1-km height (where q is specific humidity). This is addressed further in the discussion and conclusions (section 7).

The moist entropy budgets of the 12-km 1.5ent and 40-km 1.5ent models have also been analyzed. The 12-km 1.5ent and 40-km 1.5ent models agree with the results above for the 4-km 3Dsmag model in terms of the $T_R[\partial\overline{s}/\partial t]$ budget term (not shown). For the NGMS terms for these 1.5ent models (not shown), there is definitely large variance in longitude, similar to the 4-km 3Dsmag. However, there is a less clear picture in terms of overall east–west gradients, with peaks at 155°E (the farthest east with significant positive MC), then small positive NGMS to the west of that, then larger NGMS around 115°E, then relatively small (or negative) values farther west (and with the largest MC in the domain still between 70° and 90°E at this time).

Figure 13 shows that there is a weak positive correlation for the 4-km 3Dsmag model between its horizontal and vertical advective entropy divergence terms, whereas the 12-km param model has no relationship at all. For the four other models (see Table 1), the 12-km 3Dsmag model is similar to the 4-km 3Dsmag model, whereas the 40-km 1.5ent and 12-km 1.5ent are similar to the 12-km param model (with no relationship), and the 40-km param model has a weak negative relationship. While this comparison indicates a difference between models with explicit versus parameterized convection, it does not correspond to MJO performance in these models.

Benedict et al. (2014) analyze GCMs with varying ability to simulate MJOs by making scatterplots and linear regressions of horizontal and vertical advective terms of moist entropy versus MC, suggesting that some models with altered convection schemes may simulate an improved MJO for the wrong reasons. In their Fig. 8, they show ERA-Interim data with the vertical component of entropy divergence increasing with MC, while the horizontal component is mostly flat. Two of their

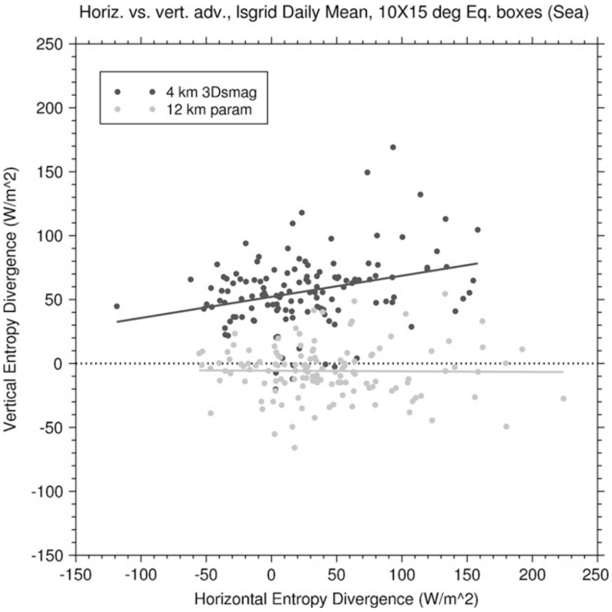

FIG. 13. Horizontal vs vertical advective terms for 4-km 3Dsmag and 12-km param runs for 10° longitude boxes covering 7.5°S–7.5°N and daily means over sea for the 10-day case study. The advective terms have been calculated using fields averaged onto a 1° grid. Linear regression fit shown for all values (solid), with regression and correlation coefficients shown in Table 1.

improved MJO models actually have the horizontal component increasing and the vertical component decreasing, which is less like ERA-Interim than the (poor MJO) control runs of those models. SPCAM, however, which also has a good MJO, looks somewhat more like ERA-Interim in their Fig. 8. We note that the model output analyzed in Benedict et al. (2014) is from global 10-yr runs, and the entropy values are more filtered and averaged in time and space than in the present study, so the comparison with our Cascade runs is not exact. However, we still see value in looking at the Cascade runs in this framework.

In this paper, we compare four "good MJO" models—the 4-km 3Dsmag, 12-km 3Dsmag, 12-km 1.5ent, and 40-km 1.5ent models—with two "poor MJO" models: the 12-km param and 40-km param models. We first show a similar analysis to that of Fig. 8 in Benedict et al. (2014) for our 10° × 15° daily means. In Fig. 14, we show regression fits for vertical and horizontal entropy advection terms versus MC for all points (dashed lines) and for only positive values of MC (solid lines), but we focus most discussion on the positive MC regressions, because they are probably more relevant for active MJO events and more comparable to the values in Benedict et al. (2014), which are taken as a large-scale average in the eastern Indian Ocean region for days with significant large-scale time-filtered rainfall.

Figure 14 shows that one main difference between the good and poor MJO models in our study is that the vertical advection term increases with MC in the good MJO models, particularly for positive values of MC (with regression coefficients ranging from 0.09 to 0.15; see Table 1), whereas the poor MJO models have somewhat smaller or negative values (0.07 and −0.02). The correlations for the vertical component in our four good MJO models (for positive MC) are also higher, ranging from 0.53 to 0.59, whereas the poor MJO models have correlations of 0.32 and −0.13.

In contrast, in Fig. 8 of Benedict et al. (2014) the regression coefficients of the vertical advective component versus MC for all MC values are 0.18 for ERA-Interim, 0.08–0.12 for the three poor MJO control simulations, 0.07 for SPCAM, and negative values for the other two good MJO models (which were speculated to have a good MJO for the wrong reasons). In other words, the preponderance of evidence from these two studies suggests that a positive regression coefficient for the vertical component versus (positive) MC values is more realistic, but it is not necessarily correlated with MJO performance, although in our study there is some relationship. In Benedict et al. (2014), the corresponding correlations (for all MC points) are 0.64 for ERA-Interim, 0.53 for the control version of the GFDL Atmosphere Model (AM3-CTL; a poor MJO model), 0.2–0.3 for the remaining poor MJO models and SPCAM, and negative for the remaining two improved MJO models. Again, the main characteristic shared by our good MJO models—relatively high correlations between the vertical entropy advection component with MC and a relatively high, positive regression slope—agrees with ERA-Interim in their study, but not with their improved MJO models in general. On the other hand, our good MJO models have horizontal advective components that increase with MC (at least for positive MC), unlike the ERA-Interim and SPCAM (for all MC) in Benedict et al. (2014).

Table 1 also includes the mean horizontal and vertical NGMS (for values with $|\mathrm{MC}| > 30\,\mathrm{W\,m^{-2}}$) for positive MC for the comparisons shown in Fig. 14 (while values for all MC are shown in Table S1 in the supplemental material). These means are calculated by first finding the ratios in each daily mean 10° × 15° box (e.g., horizontal advective term divided by MC) for all boxes satisfying the relevant MC inequality and then averaging these ratios. The positive MC regimes are again presumed to be more similar to those looked at in Benedict et al. (2014), although they were looking at averages over a single large horizontal region with particular MJO phases and smoothing in time. In that study, their Fig. 7 shows a negative relationship between east–west MJO precipitation power ratio (a measure of MJO strength and

TABLE 1. Linear regression coefficients *m* and correlation coefficients *r* for various moist entropy budget terms (or combinations of terms) from Eq. (6) regressed on MC for MC > 0, along with mean values of these terms normalized by MC (for MC > 30 W m^{-2}) for each model version; the first two rows of values are for the regression of horizontal vs vertical entropy divergence from Fig. 13. Note that the signs of terms including advection are opposite to those in Eq. (6) to be consistent with definitions of NGMS.

	4-km 3Dsmag	12-km 3Dsmag	12-km param	40-km param	12-km 1.5ent	40-km 1.5ent
$T_R[\rho\overline{\mathbf{v}}\cdot\nabla\overline{s}]$ vs $T_R[\rho\overline{w}(\partial\overline{s}/\partial z)]$						
m	0.17	0.11	0.00	−0.12	−0.01	−0.03
r	0.30	0.26	−0.01	−0.27	−0.03	−0.08
$T_R[\rho\overline{\mathbf{v}}\cdot\nabla\overline{s}]$ vs MC						
Mean Γ_H	0.16	0.21	0.33	0.18	0.37	0.33
m	0.06	0.06	0.10	0.15	0.03	0.04
r	0.19	0.18	0.18	0.32	0.06	0.09
$T_R[\rho\overline{w}(\partial\overline{s}/\partial z)]$ vs MC						
Mean Γ_V	0.64	0.19	−0.09	−0.11	−0.07	−0.13
m	0.10	0.09	0.07	−0.02	0.15	0.12
r	0.54	0.59	0.32	−0.13	0.60	0.53
$T_R[\rho\overline{\mathbf{v}}\cdot\nabla\overline{s}] + T_R[\rho\overline{w}(\partial\overline{s}/\partial z)]$ vs MC						
Mean Γ_T	0.54	0.40	0.24	0.07	0.30	0.20
m	0.16	0.15	0.16	0.13	0.18	0.16
r	0.38	0.35	0.28	0.27	0.33	0.29
[LW] + [SW] vs MC						
Mean $-\Gamma_R$	−0.73	−0.51	−0.68	−0.94	−0.48	−0.47
m	0.08	0.08	0.13	0.07	0.14	0.11
r	0.60	0.69	0.76	0.65	0.69	0.67
LH + SH vs MC						
Mean $-\Gamma_{\mathrm{SF}}$	1.10	0.82	1.02	0.97	0.94	0.81
m	0.01	−0.01	0.02	0.05	−0.03	0.00
r	0.04	−0.04	0.09	0.26	−0.12	−0.02
$T_R[\rho\overline{w}(\partial\overline{s}/\partial z)] - ([\mathrm{LW}] + [\mathrm{SW}])$ vs MC						
Mean $\Gamma_V + \Gamma_R$	1.11	0.70	0.59	0.83	0.41	0.34
m	0.03	0.01	−0.06	−0.10	0.01	0.01
r	0.18	0.10	−0.32	−0.52	0.06	0.03
$T_R[\rho\overline{\mathbf{v}}\cdot\nabla\overline{s}] + T_R[\rho\overline{w}(\partial\overline{s}/\partial z)] - ([\mathrm{LW}] + [\mathrm{SW}])$ vs MC						
Mean $\Gamma_T + \Gamma_R$	1.27	0.91	0.92	1.01	0.79	0.66
m	0.09	0.07	0.04	0.06	0.04	0.05
r	0.24	0.20	0.07	0.14	0.09	0.10
$T_R[\partial\overline{s}/\partial t]$ vs MC						
Mean $\Gamma_{\overline{s}_t}$	0.04	0.05	0.12	0.06	0.22	0.20
m	0.01	−0.01	0.03	0.03	−0.03	−0.02
r	0.04	−0.02	0.07	0.10	−0.09	−0.05

propagation in the models) and the mean vertical component of NGMS. Our values for the mean vertical component of NGMS, however, do not seem to correlate with MJO performance: the four good MJO models have mean Γ_V (for MC > 30 W m^{-2}) of 0.64, 0.19, −0.13, and −0.07, while the two poor MJO models have values of −0.09 and −0.11. The mean Γ_H and Γ_T values (for MC > 30 W m^{-2}) seem similarly unrelated to MJO performance (see Fig. S17 in the supplemental material for scatterplots and linear regression plots of total advective entropy divergence versus MC). It is difficult to draw definitive conclusions from this analysis when comparing our study with theirs.

It is worth speculating why a significantly correlated, positive relationship between the vertical component of moist entropy divergence and MC might be important for improved MJO simulation. Moisture-mode theories for the MJO attempt to explain the growth of moist entropy anomalies, for instance, by LH and LW feedbacks in areas of active convection, as well as the propagation of these anomalies eastward, for instance, by the horizontal advection term (e.g., Sobel et al. 2014). The vertical advection term tends to mainly damp *s* anomalies, since it generally exports more entropy in active convective regions and is fairly symmetric with respect to MJO phase (e.g., Chikira 2014), although it can also be somewhat asymmetric, exporting more entropy at and behind/after the peak active region (e.g., Sobel et al. 2014, their Fig. 3). One possible connection between our finding and moisture mode ideas is that the increased divergence of moist entropy at high MC values would lead to a reduced total entropy in currently

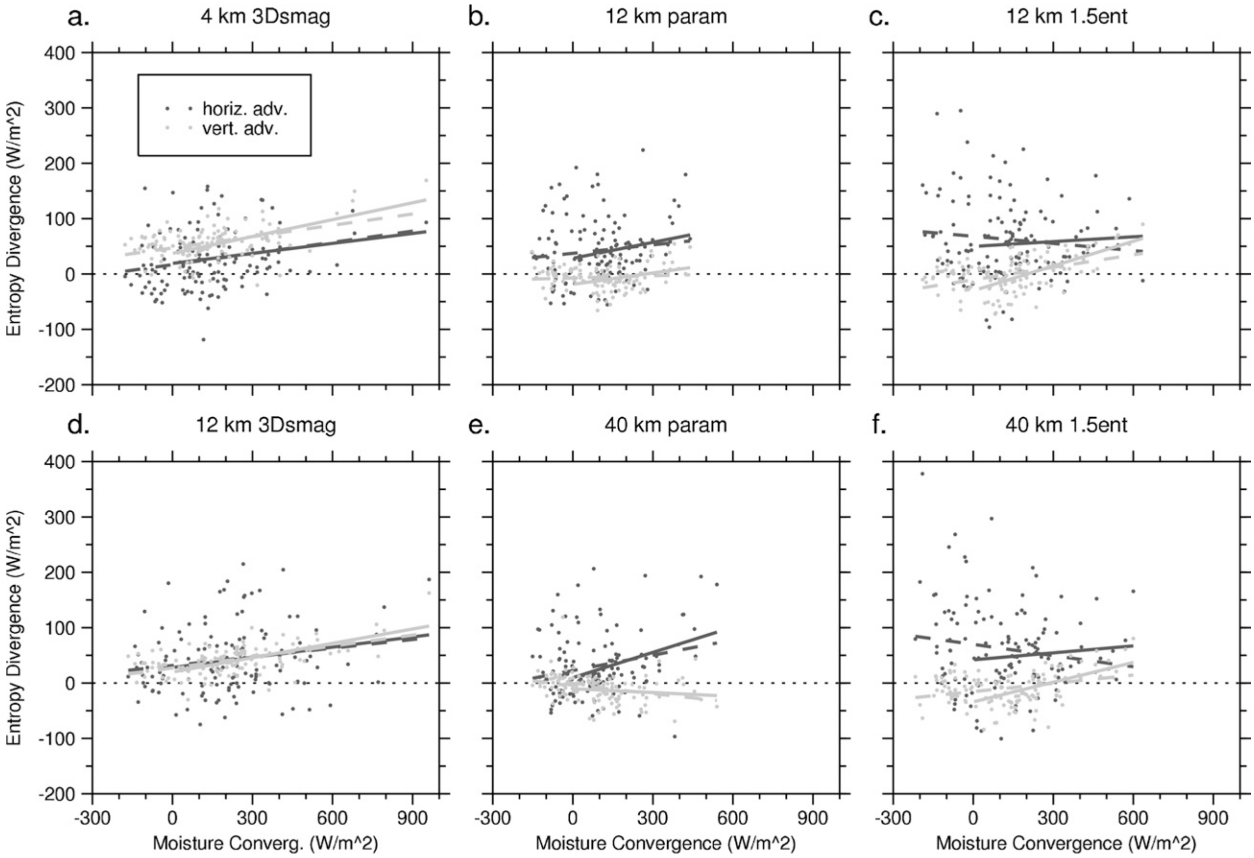

FIG. 14. Horizontal (black) and vertical (gray) advective terms plotted against MC for (a) the 4-km 3Dsmag, (b) the 12-km param, (c) the 12-km 1.5ent, (d) the 12-km 3Dsmag, (e) the 40-km param, and (f) the 40-km 1.5ent models for 10°-longitude boxes covering 7.5°S–7.5°N and daily means over sea for the 10-day case study. The advective terms have been calculated using fields averaged onto a 1° grid. Linear regression fit shown for all values (dashed) and for only values with positive MC (solid), with regression and correlation coefficients and mean Γ_H and Γ_V for positive MC shown in Table 1 (and for all values in Table S1).

active regions, allowing the propagation of the MJO to areas that currently have less MC but larger entropy (which would tend to be to the east for the theory to hold). But this requires a decrease in total entropy at high MC values, so other terms in the budget and their relationships to MC also need to be accounted for. One is the horizontal component of moist entropy divergence, which increases with MC (at least for positive MC values) for all models in our study. The other main terms are surface heat fluxes and radiation. The total surface flux shows little relationship to MC (Table 1). (Note that the slopes and correlations for surface fluxes and radiation are, with respect to sources of moist entropy, not sinks as in the case of NGMS, so a positive slope would have the opposite effect on total $T_R[\partial\overline{s}/\partial t]$ as a positive slope in NGMS.)

Radiative sources of moist entropy, on the other hand, show a very large positive relationship with MC for all models (Table 1), meaning that there is significantly less radiative cooling (or more anomalous warming) at larger MC values, most likely because of increased cloud and humidity at those times and locations. For positive MC values, the correlation coefficients range from 0.60 to 0.76, and slopes range from 0.06 to 0.14, with no systematic relationship between these values and MJO performance, unlike Benedict et al. (2014), who found that two of their modified GCMs with improved MJO performance had lower slope values for radiation versus MC (0.06 and 0.08) than ERA-Interim, SPCAM, and the poor MJO control models (0.13–0.18, their Fig. 12). Hannah and Maloney (2014) similarly find that GCMs with modified convective parameterizations and improved MJOs have too-weak cloud–radiative feedbacks that are apparently compensated by too-strong vertical advection of moist entropy.

Chikira (2014) argues that the anomalous vertical velocity induced by anomalous radiative warming can be important in allowing for anomalous moistening in active regions of the MJO. Adding [LW] and [SW] to $-T_R[\rho\overline{w}(\partial\overline{s}/\partial z)]$ in Eq. (6) will allow the dry entropy component of the vertical advection due to radiation-driven vertical velocity to cancel with radiative entropy change [assuming weak temperature gradient (WTG); Sobel et al. 2001], leaving only the effect of radiation-driven vertical velocity on vertical moisture advection in addition to the full advection by the nonradiation-driven vertical velocity. To test whether this metric, related to the ‘‘effective gross moist stability’’ (Su and Neelin 2002), helps differentiate models with good versus poor MJO performance, as suggested by Chikira (2014) (but here in a vertically integrated sense), we have computed the sum of the vertical entropy divergence and radiative entropy divergence (-1 times the three terms listed above) and plotted this against MC (see Fig. S18 in the supplemental material). We have also computed the equivalent mean NGMS as well as the slopes and correlations of the linear regressions for $\mathrm{MC} > 0$ and placed these values in Table 1 (while values for all MC are shown in Table S1 in the supplemental material). This analysis shows that, although the addition of radiation reduces the slope of entropy divergence versus MC (compared with vertical divergence only), the overall pattern found using vertical divergence alone holds for the different models. In fact, the slope for $\mathrm{MC} > 0$ for the sum of vertical plus radiative divergence is more similar than for vertical divergence alone among the four good MJO models (and also more similar among the two poor MJO models, which are both lower than the good MJO models), since the models with somewhat larger slopes in each of the two groups (the 12-km param and both 1.5ent models) also have larger radiative entropy slopes, which tend to cancel (see the entries for these subgroups in Table 1). On the other hand, the mean NGMS value (for $\mathrm{MC} > 0$) for this quantity is not related to MJO performance, similar to the vertical NGMS, and, in this case, it does not even differentiate explicit versus parameterized convection.

Given these relationships, we next compare the sum of the three terms that vary systematically with MC in the different models (horizontal, vertical, and radiative divergence) to see whether the moisture-mode idea still holds true (or whether terms are compensating each other). We also look at total change in entropy $T_R[\partial\overline{s}/\partial t]$ versus MC. These relationships are shown in Fig. 15 and Table 1. Overall correlations are very low, and the regressions may be strongly influenced by a few outliers, so it is difficult to make any strong conclusions. All of the models have positive slopes of the three-term sum versus MC (for positive MC values), meaning increasing moist entropy export from the sum of these terms at higher MC values. However, if this relationship dominated the $T_R[\partial\overline{s}/\partial t]$ relationship to MC, we would expect to see decreasing values of $T_R[\partial\overline{s}/\partial t]$ with increasing MC. In fact, we see either very small (0.01 for the 4-km 3Dsmag model) or negative slopes for this relationship in all the good MJO models, whereas the slope is 0.03 for the poor MJO models (albeit with very low correlations). This small positive relationship between MC and total entropy change in the poor MJO models might reflect their relative difficulty in simulating an eventual reduction in convection for regions that have been initialized with convection, which in turn relates to their reduced MJO propagation. However, since there are not obvious differences in the relationship between the sum of advective and radiation terms, this difference between the models in $\partial\overline{s}/\partial t$ must come from differences in surface fluxes or residual terms. Again, given uncertainties in our budgets and the low correlation coefficients, we cannot make strong conclusions regarding these relationships.

7. Discussion and conclusions

We have compared six limited-area simulations, including two with explicit convection, of a 10-day MJO case from April 2009. H13 showed that the two explicit convection simulations in the present study, the 4-km 3Dsmag and 12-km 3Dsmag models, had significantly better MJO amplitude and propagation compared with the two parameterized simulations, the 12-km param and 40-km param models.

In this paper, we first compare the moisture budgets of the 4-km 3Dsmag model and 12-km param model, finding that moisture convergence mostly balances total convective heating as expected. The net change in CWV, which is a small difference between large, compensating terms, mostly shows net moistening over most of the eastern half of the domain and net drying in the west for both models, suggesting that this feature, favoring eastward propagation on large scales, may be constrained by the lateral boundary forcing. However, there are significant differences between the models in and around convective regions leading to moistening just to the east of the convection in the 4-km 3Dsmag model, and drying behind this, roughly between 70° and 110°E. If the moisture budget relates to the difference in the MJO performance between these two model runs, it appears to show up in these subtle, regional differences.

We also compare these two models in terms of the shapes of heating and vertical velocity profiles (and in the supplemental material we show similar analyses from the other four models, including two models with parameterized convection but increased mixing entrainment and detrainment that leads to improved MJO performance, as well as observations from TOGA COARE and DYNAMO). The subgrid heating profile shapes of the 4-km 3Dsmag model are more similar to each other across different bins of vertically averaged heating,

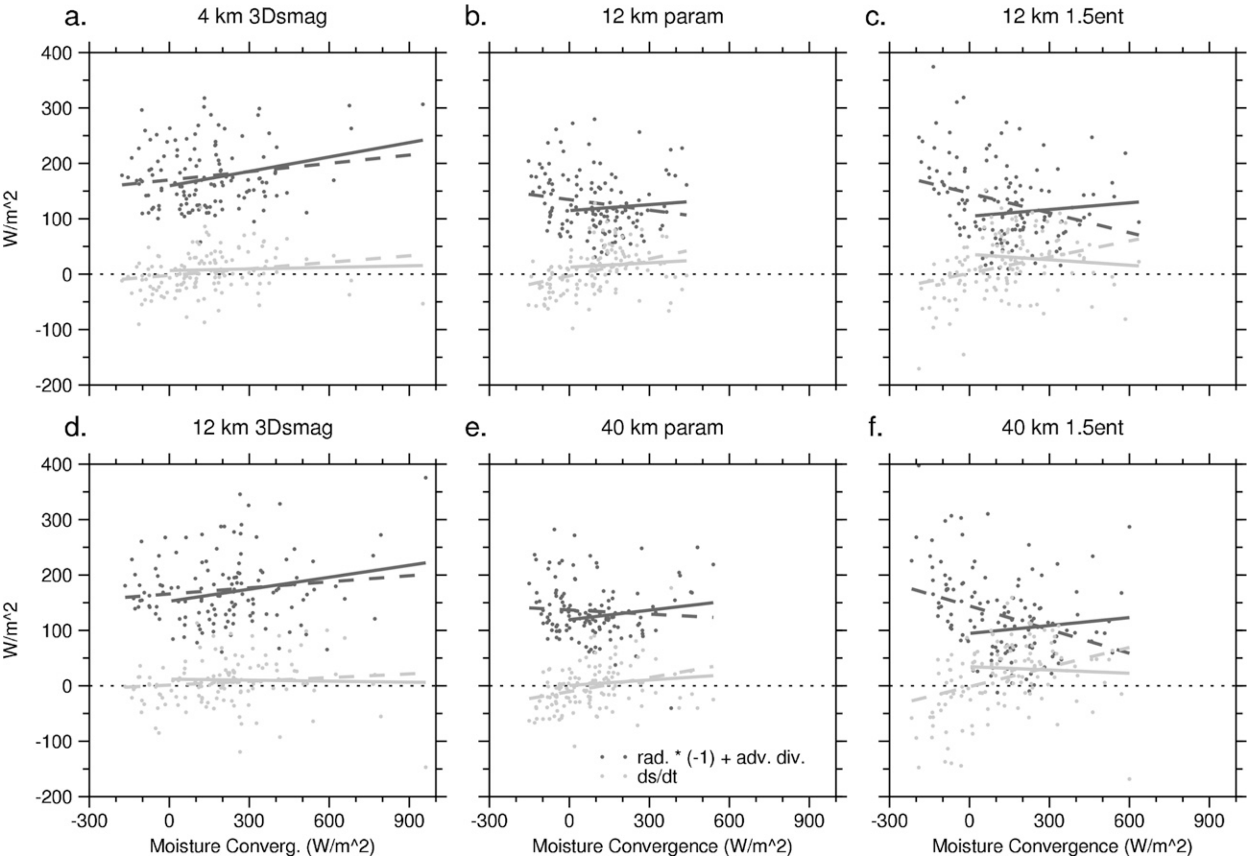

FIG. 15. The sum of horizontal and vertical advective entropy divergence and radiation entropy divergence (black), and change in entropy ($\times T_R$; gray), plotted against MC for (a) the 4-km 3Dsmag, (b) the 12-km param, (c) the 12-km 1.5ent, (d) the 12-km 3Dsmag, (e) the 40-km param, and (f) the 40-km 1.5ent models for 10°-longitude boxes covering 7.5°S–7.5°N and daily means over sea for the 10-day case study. The advective terms have been calculated using fields averaged onto a 1° grid. Linear regression fit shown for all values (dashed) and for only values with positive MC (solid), with regression and correlation coefficients and mean normalized quantities for positive MC shown in Table 1 (and for all values in Table S1).

whereas the 12-km param model has heating profiles that are less top-heavy than the 4-km 3Dsmag profiles for lower vertically averaged heating (which occurs more frequently in that model) and much more top-heavy in higher, much less frequent heating bins. This may mean that it is more difficult for the 12-km param model to transition from strong to weak convection or vice versa, reducing its ability to have propagating convection. For instance, the 12-km param model has too much light rain and not enough heavy rain (H12; H13), and these less-top-heavy heating profiles at low, preferred rain rates will help sustain convection by maintaining high CWV (and moist entropy) in light rain regions. While rare heavy rain events in the 12-km param model have very top-heavy heating, which one might think would tend to dry the column and prevent further development, in fact, we show in our moist entropy budget analysis that the vertical component of NGMS is, in general, much lower for the 12-km param model than for the 4-km 3Dsmag model, even in some of the fairly heavy rainfall regions, such as 70°–80°E. This apparent discrepancy, and our findings relating to the mean Γ_V as compared with findings in other studies, is discussed more below.

The shapes of the heating structures also differ in the lower troposphere between the two models, with the vertical gradient in normalized heating between 0- and 4-km height increasing with vertically averaged heating in the 4-km 3Dsmag model and decreasing with vertically averaged heating in the 12-km param model (mainly because of cooling from the melting and evaporation of hydrometeors in the large-scale precipitation scheme in that model that is not compensated by extra heating from the convection scheme). A metric representing this lower-tropospheric normalized heating gradient shows larger values in the moist Kelvin wave for the 4-km 3Dsmag model compared with most other regions in that model (even when accounting for the apparent dependence on vertically averaged heating discussed above), suggesting that this metric is well correlated with the propagating convective envelope in this model. In the 12-km param model, this metric is mainly a function of longitude (and, indirectly, of vertically averaged heating, as mentioned above), with regions in the eastern half of the domain showing larger values associated with less cooling from melting and evaporation of hydrometeors from the large-scale precipitation scheme in those regions. However, a similar metric for the vertical gradient of normalized vertical velocity in the lower troposphere does not show these relationships, meaning that there is not a simple mechanism connecting the heating shape with vertical velocity and low-level convergence, so the mechanism by which this would affect MJO propagation is not clear. Some possible mechanisms, which are not analyzed here but might benefit from future work, include the effects of low-level heating shapes on equatorial waves or convective momentum transport or the effects of lower-tropospheric stability on convective triggering. The excess low-level cooling in the 12-km param model also seems to feed back on the s profile and, therefore, on Γ_V, as discussed below.

The 4-km 3Dsmag model also has deep-tropospheric heating and vertical velocity profiles that are more top-heavy near and to the west of the active moist Kelvin wave associated with the MJO, whereas the 12-km param model does not have an obvious relationship between top-heaviness and organized convection other than a simple increase in top-heaviness with vertically averaged heating. This suggests a possible way that the 4-km 3Dsmag model could reduce entropy near and to the west of convection, although Γ_V does not show a consistent relationship with this metric of tropospheric top-heavy heating or vertical velocity in either model. In fact, despite the 12-km param model's more top-heavy heating and vertical velocity in the rare areas of high vertically averaged heating, these areas are shown to have relatively small Γ_V in some cases (notably, the 70°–80°E region). After investigating this further, we have found evidence that this discrepancy is due to the moist entropy profile, and mainly the temperature profile, in the lower 4 km of the troposphere. In the parameterized convection models, s peaks somewhat higher up than in the explicit convection models in regions with significant rainfall and heating, and $\partial s/\partial z$ is lower from 1- to 4-km height (while w increases upward in the lower troposphere). This is largely because $\partial\theta/\partial z$ is smaller around 2–4-km height in the parameterized models (although, around 1-km height, the main contribution to lower $\partial s/\partial z$ in the parameterized models comes from a more negative $\partial q/\partial z$). The net effect of this is that $w\partial s/\partial z$ is smaller around 1–4-km height in the parameterized convection models compared with the explicit convection models. Most of this effect (the dry entropy advection approximated by $\Pi w\partial\theta/\partial z$) can be seen in Figs. 4g and 4h and the bottom rows in Figs. S5, S8, and S9.

Comparisons with the other four models and comparisons between all six models analyzed using Q_1 (which includes radiation) rather than Q_C and with observations from TOGA COARE and DYNAMO show that the explicit convection models and, at least in the lower troposphere, the 1.5ent models, have a more realistic vertical structure of heating, vertical velocity, and vertical advective cooling for a range of heating bins (see the supplemental material). The two param models are quite similar, as are the two 3Dsmag models, whereas the 12-km param model is very different from the 12-km 3Dsmag model, despite having the same grid spacing; this is expected from H12 and H13 and shows the importance of the representation of convection. The 1.5ent models in Figs. S6 and S10 show lower-tropospheric profiles of $\Pi w\partial\theta/\partial z$ that often have local minima around 4-km height, similar to the parameterized convection models, but to a lesser extent, and the actual magnitude of the values from 1- to 4-km height are closer to the explicit convection models and observations.

We also investigate the moist entropy budget differences, and differences in NGMS, between the 4-km 3Dsmag model and the 12-km param model. Again, while the evolution of the moist entropy on the largest scales of the domain are fairly similar between the two models (with increases in the eastern half of the domain, as with CWV), there are significant differences in and around the regions of high convection in the central and eastern Indian Ocean and western Maritime Continent. When NGMS terms are compared, Γ_T in the 4-km 3Dsmag model is higher than Γ_T in the 12-km param model in the 70°–80°E region even before the CWV and moist entropy differences in the models begin, meaning that higher NGMS leads the reduction of convection in the 4-km 3Dsmag model. However, Γ_T is also higher in the 4-km 3Dsmag model in most places and times just to the east, around 90°–110°E and days 3–5, where the convection then propagates in the 4-km 3Dsmag model, so the increase in moist entropy there relative to the 12-km param model is due to something other than Γ_T values. The surface flux terms and radiation terms both contribute to slightly higher moist entropy increments in the 4-km 3Dsmag model at these locations and times (not shown), suggesting a somewhat complicated explanation for these differences. Overall, there is slightly higher total NGMS in western parts of the domain and lower total NGMS in the eastern quarter of the domain in the 4-km 3Dsmag model, although the differences in the models do not smoothly track the differences in convection and MJO propagation.

Finally, we compare all six models using an analysis of the relationship between moist entropy budget terms and MC, along with mean NGMS terms, similar to Benedict et al. (2014). Although the comparison with that paper is difficult because of different types of model, length of run times, and averaging scales, we feel that there is value in using these approaches to test moisture-mode ideas over a range of model frameworks. Our results are somewhat inconclusive, with the most robust finding being that models with relatively good MJO strength and propagation have a larger increase of the vertical component of entropy advection with increasing MC (and higher correlation coefficients for this relationship), while there is a less clear connection between MJO performance and the dependence of the horizontal component of entropy advection on MC. While this agrees with ERA-Interim and SPCAM in Benedict et al. (2014), it also agrees with their control simulations, which had poor MJO performance, suggesting that it is likely to be a physically realistic relationship but that it may not be key for MJO development. Indeed, two of the good MJO models in Benedict et al. (2014) do not have this relationship, although those were suspected in that paper of getting the MJO right for the wrong reasons. On the other hand, all of our simulations had increasing Γ_H with increasing MC (for positive MC values), while ERA-Interim and SPCAM in Benedict et al. (2014) had a flat relationship between these quantities.

We also found no correspondence between the regression coefficient of radiative warming on MC and MJO performance; this agrees somewhat with Benedict et al. (2014) and Hannah and Maloney (2014), although they argue that models with a good MJO because of higher entrainment parameters tend to have too-strong positive feedbacks (or the wrong-sign feedback) between convection and moist entropy convergence by vertical advection that are compensated by too-weak radiative feedbacks (and too-strong moist entropy export by horizontal advection), again implying that these models were getting a good MJO for the wrong reasons. Analysis of the sum of the vertical component of entropy advective divergence and the radiative entropy divergence, in which the dry entropy advection by the radiatively forced vertical velocity should cancel with the radiative entropy divergence (cf. Chikira 2014), results in a regression coefficient (when regressed on MC for positive MC values) that somewhat better differentiates the good MJO and poor MJO models, with the latter having more negative slopes.

There is also a slightly positive increase in $\partial\overline{s}/\partial t$ for the poor MJO models, whereas the other models have a slightly negative or flat relationship. This might reflect the difficulty of the poor MJO models in simulating a decrease in convection in regions where convection is initialized.

Our study shows no correspondence between MJO performance and the mean vertical NGMS Γ_V (either including negative MC values or using only positive MC values), nor do we find a correspondence with mean Γ_H, Γ_T, $\Gamma_V + \Gamma_R$, or $\Gamma_T + \Gamma_R$. This disagrees with the work of Benedict et al. (2014), who found that the three good MJO models (which had larger, more realistic east-to-west MJO-related spectral power ratios) in their study had lower mean Γ_V (and Γ_T) in the Indo-Pacific warm pool region, more similar to that of ERA-Interim. Jiang et al. (2015) also found a significant negative correlation between MJO performance and mean Γ_V (although not Γ_T) in an intercomparison of 20-yr simulations of a number of climate models. Maloney et al. (2014) also found this relationship in terms of models' ability to simulate eastern Pacific intraseasonal variability.

Why might our results be different with regard to mean Γ_V? The most obvious reason is that our single 10-day case study, with forced lateral boundary conditions, may be too different from free-running GCMs to make a useful comparison. These models are being run inside ECMWF lateral boundaries and are initialized from ECMWF analyses, so they are not able to adjust to their own preferred climatologies. The case itself is during a single MJO event, which creates sampling bias. As discussed above, Γ_V and even Γ_T are only part of the story, and it is their values at specific locations and times (along with other moist entropy budget terms) that ultimately determine the evolution of moist entropy and its relationship to regions of convection.

We suggest caution in calculating grid-scale moist entropy advective terms and NGMS terms because of the effects of local convective circulations. When calculating the advective terms using fields output on the original grids, rather than fields averaged to a 1° grid, the explicit convection models had much larger horizontal components of entropy advection (and proportionately smaller vertical components), although the total advection was very similar. When we looked into this further, we found that it was not just the grid-scale wind fields but their collocation with grid-scale moist entropy fields that led to this issue in the explicit convection runs, most likely because vertical gradients of entropy are smaller, and small-scale low-level horizontal gradients are larger, in explicit convective cells.

Comparing the results in this paper to those found in H12 and H13, we again note the preponderance of light rain (and lower vertically averaged heating and MC) in the 12-km param model. This may not be the main reason that the 12-km param model (and 40-km param model) has poor MJO performance, but it was shown to reduce the generation and conversion of eddy-available potential energy in H13. In the present study, this behavior is associated with a heating shape profile that is less top-heavy on average in the 12-km param and 40-km param models (which agrees with standard deviations of heating profiles in Fig. 10 of H13). H12 and Kim et al. (2012) show how this behavior can result in weaker circulations and less-organized convection in general. H13 also pointed to the moisture–convection relationship as a potential source of difference between the good and poor MJO models; here, advective terms of the moisture and moist entropy budget are shown to be important in how moisture evolves with convection and the MJO, though other factors also probably play a role.

There are many questions that remain in the study of the MJO and its relationship to convective-scale processes. The suggestion in Benedict et al. (2014) that at least some models with traditional convective parameterizations that have been altered to increase the sensitivity of convection to free-tropospheric moisture, and which, thereby, have improved MJOs, may be getting improved MJOs for the wrong reasons still seems plausible, although models may be wrong in different ways. The heating profiles in the explicit convection simulations seem simpler in shape and more constant (on average) with changing MC, and this agrees with observations; it would be useful to have more comparisons between explicit convection (and large-eddy simulation) runs and parameterized runs with similar forcing to investigate this further. The evidence is building that models should be able to simulate an increased vertical component of moist entropy advection with increased MC, and this should also be studied further in order to improve parameterizations. Overall, progress will be made by combining several approaches across a range of model complexities informed by insight gained from processes observed to be important for the MJO in nature and incorporating multiple scales as much as possible.

Acknowledgments. We have used ECMWF operational analyses from the YOTC online archive. We thank Jim Benedict and Dave Raymond for useful discussions and two anonymous reviewers for helpful comments that lead to significant improvements of this paper. This work made use of the facilities of HECToR, the United Kingdom's national high-performance computing service, which is provided by UoE HPCx Ltd. at the University of Edinburgh, Cray Inc., and NAG Ltd., and funded by the Office of Science and Technology through EPSRC's High End Computing Programme. This research was carried out with funding from U.K. NERC Grant NE/E00525X/1 and U.K. NERC Grant NE/I021012/1. The Cascade MetUM simulation data are available through the NERC Centre for Environmental Data Archival (CEDA) (http://catalogue.ceda.ac.uk/uuid/20981e3052a66ca71c2ba92b94760150).

REFERENCES

Benedict, J. J., E. D. Maloney, A. H. Sobel, and D. M. W. Frierson, 2014: Gross moist stability and MJO simulation skill in three full-physics GCMs. *J. Atmos. Sci.,* **71,** 3327–3349, doi:10.1175/JAS-D-13-0240.1.

Chikira, M., 2014: Eastward-propagating intraseasonal oscillation represented by Chikira–Sugiyama cumulus parameterization. Part II: Understanding moisture variation under weak temperature gradient balance. *J. Atmos. Sci.,* **71,** 615–639, doi:10.1175/JAS-D-13-038.1.

Ciesielski, P. E., R. H. Johnson, P. T. Haertel, and J. Wang, 2003: Corrected TOGA COARE sounding humidity data: Impact on diagnosed properties of convection and climate over the warm pool. *J. Climate,* **16,** 2370–2384, doi:10.1175/2790.1.

——, and Coauthors, 2014: Quality-controlled upper-air sounding dataset for DYNAMO/CINDY/AMIE: Development and corrections. *J. Atmos. Oceanic Technol.,* **31,** 741–764, doi:10.1175/JTECH-D-13-00165.1.

CSU DYNAMO, 2014: Array-averaged products, version 3B. Colorado State University, accessed 25 January 2015. [Available online at http://johnson.atmos.colostate.edu/dynamo/products/array_averages/index.html.]

CSU TOGA COARE, 2002: Version 2.1 IFA-averaged fields for TOGA COARE in support of Single Column Models. Colorado State University, accessed 25 January 2015. [Available online at http://johnson.atmos.colostate.edu/togadata/ifa_data.html.]

Davies, T., M. J. P. Cullen, A. J. Malcolm, M. H. Mawson, A. Staniforth, A. A. White, and N. Wood, 2005: A new dynamical core for the Met Office's global and regional modelling of the atmosphere. *Quart. J. Roy. Meteor. Soc.,* **131,** 1759–1782, doi:10.1256/qj.04.101.

DeMott, C. A., C. Stan, D. A. Randall, and M. D. Branson, 2014: Intraseasonal variability in coupled GCMs: The roles of ocean feedbacks and model physics. *J. Climate,* **27,** 4970–4995, doi:10.1175/JCLI-D-13-00760.1.

Grabowski, W. W., and M. W. Moncrieff, 2004: Moisture–convection feedback in the tropics. *Quart. J. Roy. Meteor. Soc.,* **130,** 3081–3104, doi:10.1256/qj.03.135.

Gregory, D., and P. R. Rowntree, 1990: A mass flux convection scheme with representation of cloud ensemble characteristics and stability-dependent closure. *Mon. Wea. Rev.,* **118,** 1483–1506, doi:10.1175/1520-0493(1990)118<1483:AMFCSW>2.0.CO;2.

Hannah, W. M., and E. D. Maloney, 2011: The role of moisture–convection feedbacks in simulating the Madden–Julian oscillation. *J. Climate,* **24,** 2754–2770, doi:10.1175/2011JCLI3803.1.

——, and ——, 2014: The moist static energy budget in NCAR CAM5 hindcasts during DYNAMO. *J. Adv. Model. Earth Syst.,* **6,** 420–440, doi:10.1002/2013MS000272.

Hirons, L. C., P. Inness, F. Vitart, and P. Bechtold, 2013: Understanding advances in the simulation of intraseasonal variability in the ECMWF model. Part I: The representation of the

MJO. *Quart. J. Roy. Meteor. Soc.,* **139,** 1417–1426, doi:10.1002/qj.2060.

Holloway, C. E., S. J. Woolnough, and G. M. S. Lister, 2012: Precipitation distributions for explicit versus parametrized convection in a large-domain high-resolution tropical case study. *Quart. J. Roy. Meteor. Soc.,* **138,** 1692–1708, doi:10.1002/qj.1903.

——, ——, and ——, 2013: The effects of explicit versus parameterized convection on the MJO in a large-domain high-resolution tropical case study. Part I: Characterization of large-scale organization and propagation. *J. Atmos. Sci.,* **70,** 1342–1369, doi:10.1175/JAS-D-12-0227.1.

Jiang, X., and Coauthors, 2015: Vertical structure and physical processes of the Madden-Julian oscillation: Exploring key model physics in climate simulations. *J. Geophys. Res. Atmos.,* doi:10.1002/2014JD022375, in press.

Johnson, R. H., and P. E. Ciesielski, 2013: Structure and properties of Madden–Julian oscillations deduced from DYNAMO sounding arrays. *J. Atmos. Sci.,* **70,** 3157–3179, doi:10.1175/JAS-D-13-065.1.

Kim, D., A. H. Sobel, E. D. Maloney, D. M. W. Frierson, and I.-S. Kang, 2011: A systematic relationship between intraseasonal variability and mean state bias in AGCM simulations. *J. Climate,* **24,** 5506–5520, doi:10.1175/2011JCLI4177.1.

——, ——, A. D. Del Genio, Y. Chen, S. J. Camargo, M.-S. Yao, M. Kelley, and L. Nazarenko, 2012: The tropical subseasonal variability simulated in the NASA GISS general circulation model. *J. Climate,* **25,** 4641–4659, doi:10.1175/JCLI-D-11-00447.1.

Klingaman, N. P., and S. J. Woolnough, 2014: Using a case-study approach to improve the Madden–Julian oscillation in the Hadley Centre model. *Quart. J. Roy. Meteor. Soc.,* **140,** 2491–2505, doi:10.1002/qj.2314.

Lean, H. W., P. A. Clark, M. Dixon, N. M. Roberts, A. Fitch, R. Forbes, and C. Halliwell, 2008: Characteristics of high-resolution versions of the Met Office Unified Model for forecasting convection over the United Kingdom. *Mon. Wea. Rev.,* **136,** 3408–3424, doi:10.1175/2008MWR2332.1.

Lock, A. P., A. R. Brown, M. R. Bush, G. M. Martin, and R. N. B. Smith, 2000: A new boundary layer mixing scheme. Part I: Scheme description and single-column model tests. *Mon. Wea. Rev.,* **128,** 3187–3199, doi:10.1175/1520-0493(2000)128<3187:ANBLMS>2.0.CO;2.

Maloney, E. D., A. H. Sobel, and W. M. Hannah, 2010: Intraseasonal variability in an aquaplanet general circulation model. *J. Adv. Model. Earth Syst.,* **2** (5), doi:10.3894/JAMES.2010.2.5.

——, X. Jiang, S.-P. Xie, and J. J. Benedict, 2014: Process-oriented diagnosis of east Pacific warm pool intraseasonal variability. *J. Climate,* **27,** 6305–6324, doi:10.1175/JCLI-D-14-00053.1.

Mapes, B., and R. Neale, 2011: Parameterizing convective organization to escape the entrainment dilemma. *J. Adv. Model. Earth Syst.,* **3,** M06004, doi:10.1029/2011MS000042.

Neelin, J. D., and I. M. Held, 1987: Modeling tropical convergence based on the moist static energy budget. *Mon. Wea. Rev.,* **115,** 3–12, doi:10.1175/1520-0493(1987)115<0003:MTCBOT>2.0.CO;2.

Pritchard, M. S., and C. S. Bretherton, 2014: Causal evidence that rotational moisture advection is critical to the superparameterized Madden–Julian oscillation. *J. Atmos. Sci.,* **71,** 800–815, doi:10.1175/JAS-D-13-0119.1.

Raymond, D. J., 2013: Sources and sinks of entropy in the atmosphere. *J. Adv. Model. Earth Syst.,* **5,** 755–763, doi:10.1002/jame.20050.

——, and Ž. Fuchs, 2009: Moisture modes and the Madden–Julian oscillation. *J. Climate,* **22,** 3031–3046, doi:10.1175/2008JCLI2739.1.

Roberts, N. M., 2003: The impact of a change to the use of the convection scheme to high-resolution simulations of convective events. Met Office Tech. Rep. 407, 30 pp.

Sobel, A. H., and E. Maloney, 2012: An idealized semi-empirical framework for modeling the Madden–Julian oscillation. *J. Atmos. Sci.,* **69,** 1691–1705, doi:10.1175/JAS-D-11-0118.1.

——, and ——, 2013: Moisture modes and the eastward propagation of the MJO. *J. Atmos. Sci.,* **70,** 187–192, doi:10.1175/JAS-D-12-0189.1.

——, J. Nilsson, and L. M. Polvani, 2001: The weak temperature gradient approximation and balanced tropical moisture waves. *J. Atmos. Sci.,* **58,** 3650–3665, doi:10.1175/1520-0469(2001)058<3650:TWTGAA>2.0.CO;2.

——, S. Wang, and D. Kim, 2014: Moist static energy budget of the MJO during DYNAMO. *J. Atmos. Sci.,* **71,** 4276–4291, doi:10.1175/JAS-D-14-0052.1.

Su, H., and J. D. Neelin, 2002: Teleconnection mechanisms for tropical Pacific descent anomalies during El Niño. *J. Atmos. Sci.,* **59,** 2694–2712, doi:10.1175/1520-0469(2002)059<2694:TMFTPD>2.0.CO;2.

Tokioka, T., K. Yamazaki, A. Kitoh, and T. Ose, 1988: The equatorial 30–60 day oscillation and the Arakawa–Schubert penetrative cumulus parameterization. *J. Meteor. Soc. Japan,* **66,** 883–901.

Waliser, D. E., and Coauthors, 2012: The ''Year'' of Tropical Convection (May 2008–April 2010): Climate variability and weather highlights. *Bull. Amer. Meteor. Soc.,* **93,** 1189–1218, doi:10.1175/2011BAMS3095.1.

Wang, S., A. H. Sobel, F. Zhang, Y. Q. Sun, Y. Yue, and L. Zhou, 2014: Regional simulation of the October and November MJO events observed during the CINDY/DYNAMO field campaign at gray zone resolution. *J. Climate,* **28,** 2097–2119, doi:10.1175/JCLI-D-14-00294.1.

Wheeler, M. C., and H. H. Hendon, 2004: An all-season real-time multivariate MJO index: Development of an index for monitoring and prediction. *Mon. Wea. Rev.,* **132,** 1917–1932, doi:10.1175/1520-0493(2004)132<1917:AARMMI>2.0.CO;2.

Wilson, D. R., and S. P. Ballard, 1999: A microphysically based precipitation scheme for the UK meteorological office unified model. *Quart. J. Roy. Meteor. Soc.,* **125,** 1607–1636, doi:10.1002/qj.49712555707.